

Diazonium-Based Covalent Molecular Wiring of Single-Layer Graphene Leads to Enhanced Unidirectional Photocurrent Generation through the p-doping Effect

Margot Jacquet,* Silvio Osella, Ersan Harputlu, Barbara Palys, Monika Kaczmarek, Ewa K. Nawrocka, Adam A. Rajkiewicz, Marcin Kalek, Paweł P. Michałowski, Bartosz Trzaskowski, C. Gokhan Unlu, Wojciech Lisowski, Marcin Pisarek, Krzysztof Kazimierzczuk, Kasim Ocakoglu, Agnieszka Więckowska, and Joanna Kargul*



Cite This: *Chem. Mater.* 2022, 34, 3744–3758



Read Online

ACCESS |



Metrics & More

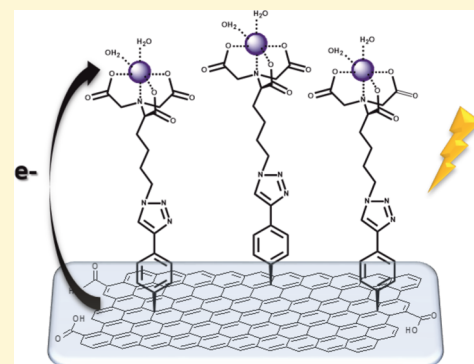


Article Recommendations



Supporting Information

ABSTRACT: Development of robust and cost-effective smart materials requires rational chemical nanoengineering to provide viable technological solutions for a wide range of applications. Recently, a powerful approach based on the electrografting of diazonium salts has attracted a great deal of attention due to its numerous technological advantages. Several studies on graphene-based materials reveal that the covalent attachment of aryl groups via the above approach could lead to additional beneficial properties of this versatile material. Here, we developed the covalently linked metalorganic wires on two transparent, cheap, and conductive materials: fluorine-doped tin oxide (FTO) and FTO/single-layer graphene (FTO/SLG). The wires are terminated with nitrilotriacetic acid metal complexes, which are universal molecular anchors to immobilize His₆-tagged proteins, such as biophotocatalysts and other types of redox-active proteins of great interest in biotechnology, optoelectronics, and artificial photosynthesis. We show for the first time that the covalent grafting of a diazonium salt precursor on two different electron-rich surfaces leads to the formation of the molecular wires that promote p-doping of SLG concomitantly with a significantly enhanced unidirectional cathodic photocurrent up to 1 $\mu\text{A cm}^{-2}$. Density functional theory modeling reveals that the exceptionally high photocurrent values are due to two distinct mechanisms of electron transfer originating from different orbitals/bands of the diazonium-derived wires depending on the nature of the chelating metal redox center. Importantly, the novel metalorganic interfaces reported here exhibit minimized back electron transfer, which is essential for the maximization of solar conversion efficiency.



INTRODUCTION

Development of well-performing functional materials covers numerous potential applications in electronic,¹ medicine,² catalysis,³ and photovoltaic⁴ fields to name a few. To achieve an efficient robust and stable final device, a rational design of the chemical interface between the working modules is essential. To this end, different strategies have been implemented depending on the final device configuration to reach a fine balance between the nanostructuring of the electrode surface and the preservation of the properties of the device modules that would ensure efficient electronic communication, high conversion efficiencies, and high product yield. Several methodologies have been employed for the modification of a wide range of materials based on the use of various types of processes, such as electrostatic interactions,⁵ chemi- and physisorption,⁶ hydrophobic interactions,⁷ van der Waals interactions, and π - π stacking.⁸ Among them, chemisorption, which ensures the formation of covalent bonds on the substrate, is a promising strategy to achieve a

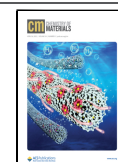
strong and stable attachment of the (photo)electroactive molecules. Depending on the materials, various molecular wiring approaches have been reported with the use of carboxylates,⁹ silanes,¹⁰ titanates,¹¹ phosphonates,¹² thiolates,¹³ and diazonium salt, as the most commonly used.

Covalent bonding using diazonium salt precursors was introduced by the Pinson group in 1992 in a pioneering study in which carbon surfaces were functionalized via the electrochemical reduction of aryl diazonium salt.¹⁴ Since then, a significant effort has been devoted to develop this highly promising advanced functional platform. In fact, the high interest in such systems is still prevailing, as shown in recent

Received: January 10, 2022

Revised: April 1, 2022

Published: April 12, 2022



reviews on the subject.^{1,15,16} The appeal of this approach is due to several factors. First, the grafting using diazonium salt is a fast and simple reaction that can be performed in a green manner using either the electrochemical,¹⁴ spontaneous,¹⁷ or photochemical approach.¹⁸ Second, the universality of the method stems from the fact that the grafting can be applied to various materials including transparent conductive oxides (TCOs: SnO₂,¹⁹ ZnO,^{4,20} FTO,²¹ and ITO^{6,22}), metals (gold,^{3,23} copper,²³ platinum,²⁴ and iron²⁵), silicon,²⁶ and allotropic forms of carbon (graphite,²⁷ glassy carbon,^{28,29} graphenoids,^{30–32} and diamond³³). Third, the strong covalent bonding achieved through diazonium grafting allows for the improved stability of the resulting nanoconstructs under ambient conditions. Importantly, it also offers a great deal of versatility toward the use of solvents, sonication,²⁸ corrosive conditions,^{34,35} high temperature,³⁶ and a wide electrochemical window,^{34,37} which are all important assets in the quest for the viable functional materials. Finally, the organic synthesis of diazonium salts can be performed in a straightforward way from anilines, which are available commercially in a great variety. These include anilines containing para-substituents suitable for further functionalization steps, particularly during the construction of complex functional materials based on the “diazonium salt coupling agents”.³⁸

Despite the numerous above-mentioned benefits of diazonium salts, there are some important limitations associated, such as the tendency to form unorganized and uncontrolled multilayers, mainly due to the high reactivity of the ensuing radicals.³⁹ To overcome this drawback and to obtain well-organized molecular architectures, various approaches have been developed that rely on the use of bifunctional aryl diazonium salts bearing bulky protective groups.^{23,40} In particular, using protected alkyne functionalities combined with the “click” chemistry involving the Huisgen 1,3-dipolar cycloaddition is a highly promising strategy.^{41,42} In addition to the green aspects of this approach, the efficient and selective “click” reaction can be performed under mild conditions with various substrates. Importantly, previous studies on the development of photo- and redox-active materials have shown that the triazole bridge formed during the latter reaction is highly stable and greatly facilitates the electron transfer process.^{43,44}

Among all the studied materials obtained by covalent grafting of diazonium salts, a strong focus has been put on graphene-based materials. As graphene is one of the most thoroughly studied materials in the last 15 years,^{45–48} it should be emphasized that in order for graphene to be successfully applied in the functional devices, it requires chemical functionalization that does not impair its intrinsic high conductance while promoting a semiconductor-like behavior. The grafting of diazonium salt-derived aryl radicals induces the re-hybridization from sp² to sp³ carbon atoms and introduces beneficial defects in the well-organized hexagonal flat lattice of graphene. This type of covalent modification has been shown to be effective for fine-tuning the band gap,⁴⁹ inducing p- or n-doping effects in graphene-based materials, resulting in the establishment of asymmetric conductance,⁵⁰ magnetism,⁵¹ and also increasing the conductivity.⁵² Of various forms of graphene, single-layer graphene (SLG) is a material of choice particularly in photovoltaic and solar-to-fuel applications, including those based on biophotocatalysts, due to high transparency and biocompatibility of this material. However, to the best of our knowledge, the influence of covalent grafting of

SLG on photocurrent generation has not been studied at the molecular level until now.

Here, we report the development of a universal well-organized metalorganic interface based on the covalent electrografting of diazonium salt and “click” chemistry on two conductive and transparent surfaces: fluorine-doped tin oxide (FTO) and FTO/SLG systems. The resulting wires contain the terminal nitrilotriacetic acid (NTA) metal complexes, which are well-known to serve as anchors for the oriented attachment of His₆-tagged proteins, including (photo)electroactive proteins. A comprehensive analysis of the photocurrent generation in conjunction with the computational analysis of electron transfer is presented, demonstrating for the first time the significantly improved unidirectional photocurrent generation. We provide the underlying molecular mechanism of this phenomenon derived from QM/MM modeling of electron transfer in the entire nanosystem.

EXPERIMENTAL SECTION

General Materials. All chemical reagents and solvents used for the synthesis were purchased from commercial sources (Aldrich, Acros, and VWR) and were used without further purification unless otherwise noted. FTO glass substrates were purchased from Sigma-Aldrich (30 mm × 30 mm and 2.2 mm thickness). Prior to use, FTO electrodes were pre-cut to a size of 15 × 15 mm for all subsequent modification steps and to a size of 7.5 mm × 7.5 mm for the secondary ion mass spectrometry (SIMS) and X-ray photoelectron spectroscopy (XPS) analyses. ¹H and ¹³C NMR spectra were recorded at 700 and 176 MHz, respectively, on an Agilent DirectDrive2 spectrometer equipped with a room-temperature HCN probe, temperature-controlled at 25 °C. Chemical shifts were calibrated to the residual solvent peak. Coupling constant values (*J*) are given in Hz and chemical shifts (δ) are given in ppm. The mass spectra were recorded with a Quattro LC mass spectrometer. EXTREME CAUTION was taken during the manipulation of imidazole-1-sulfonyl azide hydrochloride, which is explosive.⁵³ The tetrafluoroborate diazonium salt is stable, but other salts can be explosive.

Preparation of SLG. The chemical vapor deposition method was used for the production of SLG. After pre-cleaning processes, the copper foil (99.999% purity) was placed in an oven, and a 30 min preheating treatment at 1000 °C under H₂ gas flow and a vacuum of 10⁻⁵ Torr was carried out. This step was applied to remove the oxide from the Cu foil surface and to ensure the growth of grains in Cu. Then, CH₄ gas, used as a carbon source, was added to the system at 50 sccm for 30 min for the production of graphene on the surface, followed by rapid cooling under a H₂ and Ar atmosphere. Finally, the SLG was transferred to precut FTO substrates (15 mm × 15 mm) and characterized by field emission-scanning electron microscopy (Figure S1) and atomic force microscopy (Figure S2).

4-((Trimethylsilyl)ethynyl)aniline (TMS-NH₂).⁵⁴ A flask was charged with bis(triphenylphosphine)palladium(II) dichloride (28 mg, 0.6 mol %) and copper(I) iodide (21 mg, 17 mol %), and under an atmosphere of argon were added a degassed solution of triethylamine (15 mL), 4-iodoaniline (1.25 g, 5.6 mmol), and trimethylsilylacetylene (0.87 mL, 6.2 mmol). The solution was stirred at room temperature under argon for 24 h. The mixture was then filtered, and the precipitate was washed with triethylamine and diethyl ether. The filtrate was washed with aqueous NH₄Cl (2 M) and brine. The organic layer was dried over Na₂SO₄ and filtered to obtain the desired compound after evaporation of the solvent (1.03 g, 97%). ¹H NMR (700 MHz, CDCl₃): δ 7.27 (d, *J* = 8 Hz, 2H), 6.57 (d, *J* = 8 Hz, 2H), 3.78 (s, 2H), 0.22 (s, 9H). ¹³C NMR (176 MHz CDCl₃) 146.9, 133.5, 114.7, 112.6, 106.1, 91.5, 31.1, 0.3. MS *m/z*: calcd for C₁₁H₁₆N₂Si⁺, 190.10 [M + H]⁺; found, 190.10.

4-((Trimethylsilyl)ethynyl)benzenediazonium Tetrafluoroborate (TMS-N₂).⁵⁴ To a degassed solution of nitrosyl tetrafluoroborate (141 mg, 1.2 mmol) in acetonitrile (2 mL) was added dropwise at -40 °C a degassed solution of TMS-NH₂ (216 mg, 1.1 mmol) in

acetonitrile (2.3 mL). The solution was stirred at $-40\text{ }^{\circ}\text{C}$ for 1 h, and diethyl ether was added. The precipitate was filtered off and washed with cold diethyl ether (211 mg, 64%). $^1\text{H NMR}$ (700 MHz, CDCl_3): δ 8.55 (d, $J = 9\text{ Hz}$, 2H), 7.77 (d, $J = 9\text{ Hz}$, 2H), 0.28 (s, 9H). $^{13}\text{C NMR}$ (176 MHz CDCl_3) 136.8, 134.3, 132.8, 112.5, 109.7, 101.8, 31.1, -0.4 . MS m/z : calcd for $\text{C}_{11}\text{H}_{13}\text{N}_2\text{Si}^+$, 201.08 $[\text{M} - \text{BF}_4]^+$; found, 201.08.

N^{α}, N^{α} -Bis(carboxymethyl)-L-azido-lysine Hydrochloride (NTA- N_3).⁵⁵ To a solution of N^{α}, N^{α} -bis(carboxymethyl)-L-lysine hydrate (1.00 g, 3.81 mmol) in water (35 mL) were added K_2CO_3 (2.40 g, 17.4 mmol) and $\text{CuSO}_4 \cdot 2\text{H}_2\text{O}$ (10 mg, 0.065 mmol). After complete dissolution, a suspension of imidazole-1-sulfonyl azide hydrochloride (950 mg, 7.62 mmol) in acetonitrile (10 mL) was added. The reaction mixture was stirred overnight at room temperature, and the solvents were removed under reduced pressure. The residue was dissolved in H_2O and acetonitrile was added (6 mL). Two different phases and a precipitate were observed, and the upper phase was discarded. A minimum amount of water was added until a clear solution was obtained; the addition of acetonitrile and removal of the upper phase was repeated three times. The lower phase was acidified to pH 2 with aqueous HCl (4 M), and acetone was added (5 mL). Two different phases and a precipitate were observed, and the upper phase was collected. The addition of acetone and collection of the upper phase was repeated three times. The combined upper phases were concentrated under reduced pressure to obtain the desired product in the form of hydrochloride salt (1.03 g, 86%). $^1\text{H NMR}$ (700 MHz, D_2O): δ 3.82–3.72 (m, 5H), 3.34 (t, $J = 6.4\text{ Hz}$, 2H), 1.96–1.79 (m, 2H), 1.68–1.47 (m, 4H). $^{13}\text{C NMR}$ (176 MHz, D_2O) 175.5, 173.1 (2C), 71.0, 58.1 (2C), 53.3, 30.4, 29.1, 26.3. MS m/z : calcd for $\text{C}_{10}\text{H}_{15}\text{N}_4\text{O}_6^-$, 287.1 $[\text{M} - \text{H}]^-$; found, 287.1.

Surface Modification. The bare material was first cleaned by ultrasonication in an acetone bath for 1 min and then was left to dry. The electrografting of TMS- N_2 (2.2 mM) in 0.1 M tetrabutylammonium hexafluorophosphate (NBu_4PF_6) in acetonitrile was performed using cyclic voltammetry (CV) at a scan rate of 50 mV/s for 1 cycle between +0.5 and -0.5 V versus Ag/AgCl. The surface was cleaned with a copious amount of acetonitrile and tetrahydrofuran, followed by immersion in a tetrabutylammonium fluoride (TBAF) solution (50 mM in THF) for 5 min. After rinsing with a copious amount of THF and water, the “click” chemistry was performed by first immersing in a degassed solution of NTA- N_3 (0.4 mM in water). A mixture of 100 μL of tris(benzyltriazolylmethyl)amine (TBTA) in DMSO (0.10 mM) and 200 μL of CuSO_4 in water (0.04 mM) was added followed by bubbling with argon for an additional 15 min. Then, 100 μL of sodium ascorbate solution in water (1.5 mM) was added, and the reaction was performed overnight under an inert atmosphere. The surface was cleaned with water and immersed in an ethylenediaminetetraacetic acid (EDTA) solution (2.5 mM in water) for 20 min. Finally, after rinsing with water, the chelation with the metal ($\text{NiSO}_4 \cdot 7\text{H}_2\text{O}$ or $\text{Co}(\text{NO}_3)_2 \cdot 6\text{H}_2\text{O}$) was conducted by immersion in an 0.1 M solution in water for 1 h with nickel and overnight with cobalt.

Secondary Ion Mass Spectrometry. SIMS measurements were performed employing a CAMECA SC Ultra instrument under an ultra-high vacuum of 4×10^{-10} mbar. The Cs^+ primary beam was rastered over $250 \times 250\text{ }\mu\text{m}$ (the analysis area was limited to $200 \times 200\text{ }\mu\text{m}$), and the positive ion detection mode was used in the experiments, and thus, all species were measured as CsX^+ cluster ions. The intensity of the primary beam was 2 pA, and the impact energy was 5 keV. To perform lateral imaging measurements, a highly uniform beam was required—the beam on the sample in the SC Ultra tool has a square shape and owing to the “variable rectangular shape concept” forms a homogeneous spot. The primary beam at the working point in SC Ultra is formed by two stencils—well-shaped apertures. While the first one is used to choose the most intense and homogeneous part of the Gaussian-shaped ion beam, the second one changes the size of the spot.

X-ray Photoelectron Spectroscopy. XPS experiments were performed in a PHI 5000 VersaProbe scanning ESCA microprobe (ULVAC-PHI, Chigasaki Japan) instrument at a base pressure below

5×10^{-9} mbar. The XPS spectra were recorded using monochromatic Al $K\alpha$ radiation ($h\nu = 1486.6\text{ eV}$) from an X-ray source operating at 100 μm spot size, 25 W, and 15 kV. Both survey and high-resolution XPS spectra were collected with the analyzer pass energy of 117.4 and 23.5 eV and the energy step size of 0.4 and 0.1 eV. Casa XPS software (v.2.3.19, Casa Software Ltd, Wilmslow, United Kingdom) was used to evaluate the XPS data. Shirley background subtraction and peak fitting with Gaussian–Lorentzian-shaped profiles were performed. The binding energy scale was referenced to the C 1s peak with BE = 284.6 eV. For quantification, the PHI Multipack sensitivity factors and determined transmission function of the spectrometer were used.

Electrochemistry. Electrochemical experiments were performed with a Metrohm Autolab B.V. potentiostat/galvanostat in a custom-made Teflon three-electrode cell under an argon atmosphere, using a glassy carbon rod as the counter electrode and an Ag/AgCl (3 M KCl) reference electrode. The FTO or FTO/SLG surface was used as a working electrode connected with a conductive adhesive copper tape (6.4 mm width, 1181, 3 M) to provide electrical contact. CV and electrochemical impedance spectroscopy measurements (EIS) were conducted in 0.1 M phosphate buffer (pH 7) with 1 mM 1,1'-ferrocenedimethanol at a scan rate of 100 mV/s (CV) and at a frequency range from 0.01 Hz to 0.1 MHz (EIS). Z-View 2 software was used to fit the impedance data with an equivalent circuit. Photoelectrochemical experiments were performed using a KL 2500 LCD halogen white light source (Schott) with a light intensity of 100 mW/cm^2 . The geometric surface area of the analyzed samples was calculated to be 0.3848 cm^2 based on the FFKM O-ring used as a hermetic seal between the surface and the electrolyte. Photochronoamperometric experiments were performed under aerobic conditions at room temperature with 5 mM phosphate buffer (pH 7) as the electrolyte. Before each measurement, the open-circuit potential was recorded under dark conditions until a stable potential was achieved. During photochronoamperometric measurements, samples were illuminated at different potentials (vs Ag/AgCl) with 30 s “light ON/OFF” periods.

Raman Spectroscopy. Raman spectra were recorded using a DXR Raman microscope (Thermo Scientific) with a 50 \times /0.75 NA objective. The exposure time was equal to 30 s, and typically 16 scans were averaged for a single spectrum. To ensure repeatability, a minimum of six spectra were collected from random spots on the sample. For each experiment, green laser ($\lambda = 532\text{ nm}$) was used as a source of excitation with 1 mW power to prevent the sample from overheating. The distance between spectral points was equal to 0.964233 cm^{-1} .

Computational Methods. To computationally model the system of interest, we used a hexagonal 2D slab of monolayer graphene with lattice parameters $a = 10.70\text{ }\text{Å}$, $b = 6.179\text{ }\text{Å}$, and $\alpha = 120^\circ$ and a C–C distance of 1.43 Å . On this supercell, one NTA-modified molecule of the self-assembled monolayer (SAM) (1-pentyl-4-phenyl-1H-1,2,3-triazole) coordinating one Ni^{2+} ion was chemisorbed on the graphene layer, and a vacuum region of 50 Å was introduced in the third dimension (z -axis) to avoid spurious electrostatic interactions between the replica. Due to the high computational cost of the optimization at the density functional theory (DFT) level for such big interfaces, a two-step procedure has been considered. In the first step, geometry optimization using a density functional tight-binding (DFTB) approach⁵⁶ with periodic boundary conditions, as implemented in DFTB+ software,⁵⁷ has been used. Such an approach has been successfully validated in our previous studies on a pyrene-NTA SAM physisorbed on SLG.^{58,59} In the second step, these optimized structures have been used as a starting point for the optimization with the DFT periodic protocol using the PWscf package of the Quantum ESPRESSO suite of programs⁶⁰ and the PBE functional.^{61,62} Ultrasoft pseudopotentials⁶³ together with a cutoff of 50 and 200 Ry for the expansion of the wave function and density were applied, respectively. The dipole correction of the electrostatic potential was taken into account to counterbalance the asymmetry arising from the formation of the SLG-SAM interface in the electrostatic potential. A $6 \times 6 \times 1$ k -sampling was used for the analysis of the Brillouin zone at the Γ point.

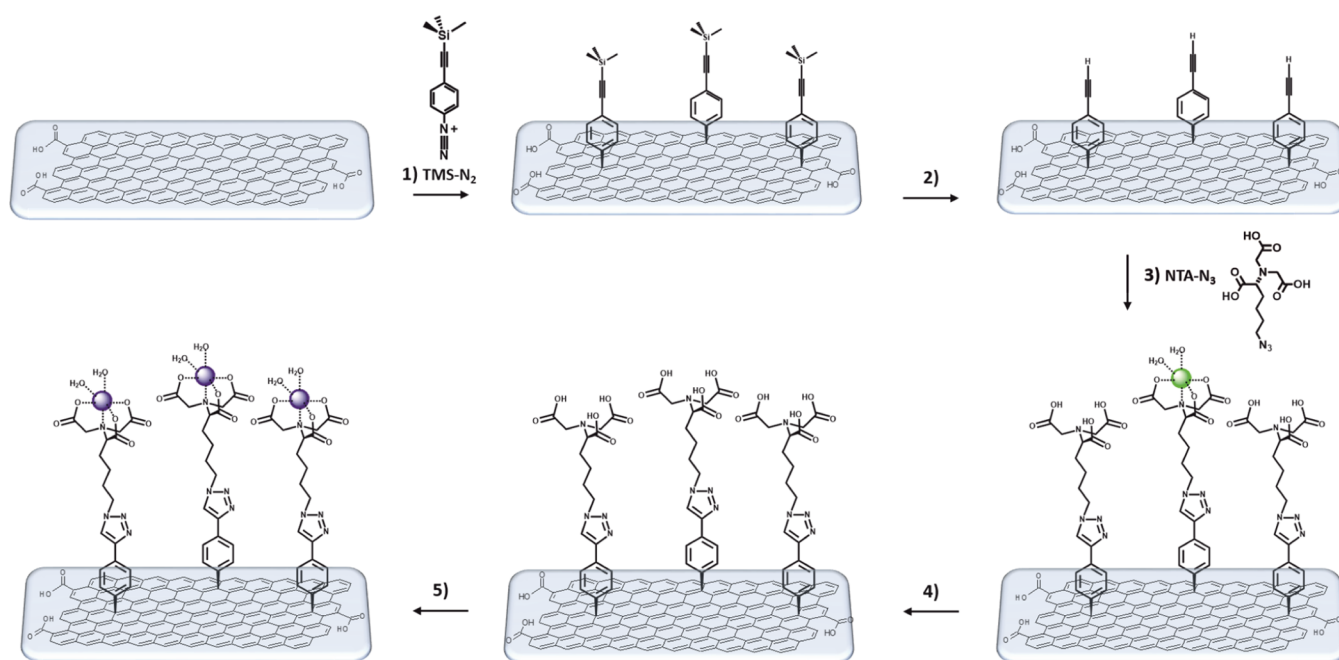


Figure 1. Stepwise preparation of functionalized FTO/SLG-cNTA-M²⁺ electrodes. (1) Electrochemical grafting of TMS-N₂ (grafted). (2) TBAF in THF (deprotected). (3) Click chemistry with NTA-N₃ (click). (4) Aqueous solution of EDTA (EDTA). (5) Metalation with either NiSO₄ or Co(NO₃)₂ (metal).

The same two-step optimization procedure was used in the study of the effect of different metals on the electron transfer ability of the interface, in which the Ni²⁺ ion was replaced with either Co²⁺ or Cu²⁺. To complete the octahedral coordination of the metals and mimic the experimental setup in which a His₆ tag is present, two imidazole molecules were added to the system (Figure S3). To preserve the neutrality of the system, which is necessary for periodic boundary condition calculations when the M²⁺ cation is present, one of the carboxylic groups was protonated.

The work function analysis has been performed with a similar methodology as reported in our previous studies on physisorption.^{58,59} Briefly, the work function shift has been defined as

$$\Delta W F = \Delta V_{S A M} + B D \quad (1)$$

where $\Delta V_{S A M}$ is the part of the shift arising from the dipole moment differences of the molecular backbone (labeled as the molecular contribution), BD is the bond dipole contribution, and the differences measured are between the converged potential on the bare side of the graphene surface and on the SAM-covered side of the surface. The first contribution ($\Delta V_{S A M}$) was estimated by computing the electrostatic potential profile across the molecules without graphene, while keeping the geometry frozen. The BD contribution to the work function shift was then calculated by subtracting $\Delta V_{S A M}$ from $\Delta W F$. In the Helmholtz model,^{64,65} the molecular contribution to the work function shift is directly proportional to the molecular dipole along the axis normal to the surface, μ_{\perp} , and inversely proportional to the surface area per adsorbed molecule A ⁶⁶

$$\Delta V_{S A M} = e \mu_{\perp} / \epsilon_0 A \quad (2)$$

with ϵ_0 being the vacuum permittivity. As a consequence, if the SAM dipole is pointing toward the metal surface, the shift in the work function is positive, while if the dipole points away from the surface, the shift in the work function is negative.^{67,68}

RESULTS AND DISCUSSION

Surface modification via covalent electrografting and “click” chemistry. The optimized functionalization of FTO and FTO/SLG surfaces was conducted in five steps (Figure 1) based on the electrografting of an aryl diazonium salt followed by a

“click” reaction with an azide derivative to introduce the NTA moiety.

As previously reported, the key importance of the construction of efficient nanodevices based on the electrografting of diazonium salts is the formation of a homogeneous monolayer devoid of radical polymerization.¹⁵ Indeed, the well-studied mechanism of diazonium grafting is based on the one-electron reduction of the diazonium in conjunction with the dinitrogen cleavage, which leads to the formation of a highly reactive aryl radical.³⁹ In order to avoid the oligomerization at the meta-position, which could affect the construct functionality, different strategies have been reported including the use of a small number of CV scans, an optimized concentration,⁶ a small potential window, and the use of bulky functional groups at the para-position.^{40,69} In our study, a combination of these approaches was used to ensure the optimal grafting of 4-((trimethylsilyl)ethynyl)-benzenediazonium tetrafluoroborate (TMS-N₂). The electrografting was performed via one CV scan at 50 mV/s between 0.5 and −0.5 V with a degassed solution of TMS-N₂ in acetonitrile/NBu₄PF₆. The corresponding CV curves obtained for the FTO and FTO/SLG surfaces are presented in Figure S4, showing a broad irreversible cathodic peak typical of the electroreduction process of the diazonium compound. The surfaces were then subjected to deprotection with a solution of TBAF in THF to remove the trimethylsilyl (TMS) function of the grafted compounds. It is important to note that in the case of the FTO/SLG electrode, the surface is highly sensitive to the latter step, and a proper balance between the concentration of grafted compounds and incubation time with TBAF solution is required. Free alkyne functions were then subjected to a subsequent “click” reaction with N^α,N^α-bis(carboxymethyl)-L-azido-lysine hydrochloride (NTA-N₃) using the Huisgen 1,3-dipolar cycloaddition to form a triazole bridge. The reaction was performed overnight in water, catalyzed by a stabilized complex of copper with TBTA, activated by sodium ascorbate.

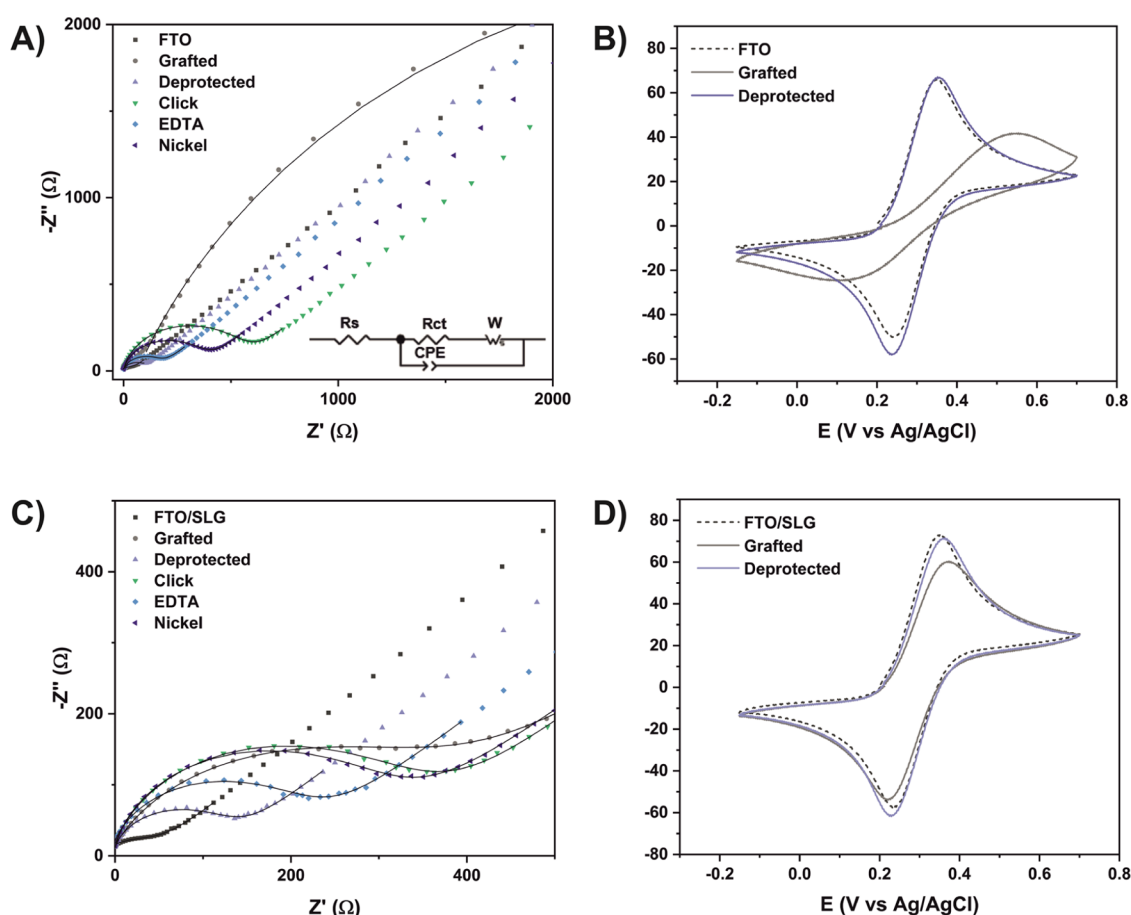


Figure 2. (A) Nyquist plot and fitted curves of electrochemical impedance spectra obtained for the FTO-cNTA-Ni electrode at different steps of functionalization. Inset: equivalent circuit model. (B) CV at 100 mV/s of FTO (dashed) after grafting (gray) and deprotection steps (blue). (C) Nyquist plot and fitted curves of electrochemical impedance spectra obtained for the FTO/SLG-cNTA-Ni electrode at different steps of functionalization. (D) CV at 100 mV/s of FTO/SLG (dashed) after grafting (gray) and deprotection steps (blue). All measurements were performed with 1 mM 1,1'-ferrocenedimethanol (exogenous redox probe) in 0.1 M phosphate buffer (pH 7).

Table 1. Curve Fitting Result of R_{ct} Based on the $R_s ((R_{ct}W)CPE)$ Model and Calculated Capacitance C_{dl} for FTO and FTO/SLG Electrodes at Each Step of Functionalization in 1 mM 1,1'-Ferrocenedimethanol + 0.1 M Phosphate Buffer (pH 7)

	FTO-cNTA-Ni		FTO-cNTA-Co		FTO/SLG-cNTA-Ni		FTO/SLG-cNTA-Co	
	R_{ct} (Ω cm ²)	C_{dl} (μ F/cm ²)	R_{ct} (Ω cm ²)	C_{dl} (μ F/cm ²)	R_{ct} (Ω cm ²)	C_{dl} (μ F/cm ²)	R_{ct} (Ω cm ²)	C_{dl} (μ F/cm ²)
bare electrode	47.9	14.0	35.7	11.0	28.3	5.3	31.1	7.4
grafted	2646.3	43.6	722.3	33.4	144.0	16.5	150.6	16.7
deprotected	49.9	11.3	36.9	10.3	48.9	8.1	66.1	7.9
click	217.6	11.8	227.1	11.8	129.7	10.2	212.6	11.3
EDTA	70.1	12.0	73.6	11.7	83.2	8.8	95.7	9.1
metal	146.3	11.5	137.3	11.0	115.0	9.0	115.3	9.1

Due to the ability of the NTA ligand to chelate copper,⁷⁰ the surfaces were treated with aqueous EDTA solution to remove the residual copper cations. Finally, the desired metalorganic wires, denominated as cNTA-Ni and cNTA-Co, were obtained by incubating the electrodes in an aqueous solution of NiSO₄ or Co(NO₃)₂ for 1 h or overnight, respectively.

Characterization of the Step-by-step Wire Construction. The methodology employed for the functionalization of the different materials was evaluated, optimized, and confirmed by the complementary application of electrochemical analyses, Raman spectroscopy, SIMS, and XPS.

Electrochemical Analyses. To dissect the step-by-step construction of the diazonium-based molecular interface, the electronic interfacial properties were studied by EIS and CV in

the presence of 1,1'-ferrocenedimethanol as an exogenous redox probe in pH-neutral electrolyte (phosphate buffer, pH 7) in a frequency range from 0.01 Hz to 0.1 MHz. The corresponding Nyquist plot with fitted curves and CV scans obtained for the FTO-cNTA-Ni and FTO/SLG-cNTA-Ni electrodes are presented in Figure 2A–DA, respectively (see Figures S5 and S6 for the data from FTO and FTO/SLG Co-based electrodes). The charge transfer resistance R_{ct} and the double-layer capacitance C_{dl} ⁷¹ of the bare and modified electrodes were calculated by fitting the EIS data with the equivalent circuit model (Figure 2A, inset), where R_s stands for the electrolyte resistance, CPE is the constant-phase element corresponding to the double-layer capacitance existing between the solid/liquid phases, R_{ct} corresponds to the charge

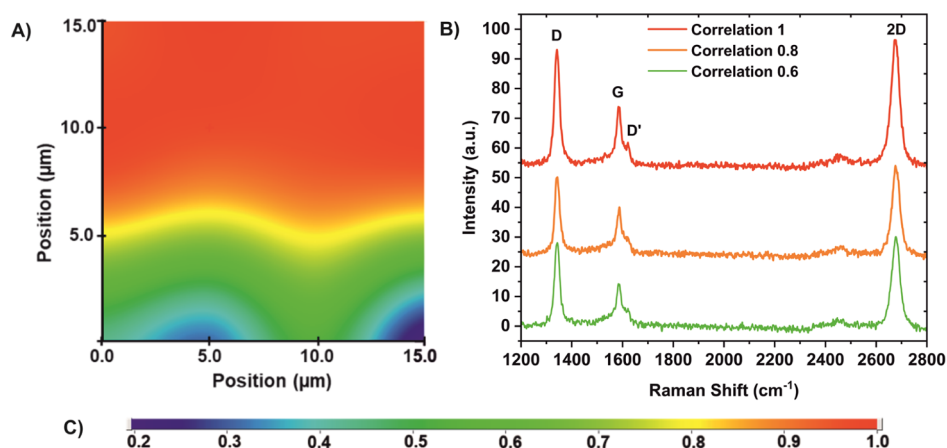


Figure 3. Raman mapping of the FTO/SLG-cNTA-Ni samples. (a) Correlation map. (b) Representative Raman spectra of the FTO/SLG-cNTA-Ni sample with a correlation of 1.0, 0.8, and 0.6. (c) Color scale of the correlation map.

transfer resistance between the electrolyte and the studied electrode, and W represents the Warburg impedance caused by the diffusion process. The obtained resistance R_{ct} and capacitance C_{dl} (from CPE parameters Q and Φ ⁷¹) values are summarized in Table 1 (see Table S1 for the complementary parameters R_s , Q , and Φ).

Despite the variability of the absolute charge transfer resistance values, the tendency observed for the R_{ct} parameter is in accordance with the different steps of functionalization and is reproducible for all the different configurations and surfaces studied here (Figure 2A,C and Table 1). Thus, bare electrodes possess a small R_{ct} value between 36 and 48 $\Omega\text{ cm}^2$ for FTO and slightly below this for the FTO/SLG electrode (around 30 $\Omega\text{ cm}^2$) due to its higher conductivity property. After the grafting of TMS-N₂, the monolayer behaves as an insulator due to the presence of the bulky TMS group, which hinders access of the redox probe to the electrode. Therefore, the R_{ct} increases drastically in the case of FTO surfaces with values around 2650 and 720 $\Omega\text{ cm}^2$. This effect is also demonstrated by the complementary CV analysis (Figures 2B and S5B), which shows the attenuation of the redox probe detection characterized by a lower peak current intensity and a higher peak-to-peak separation. In the case of FTO/SLG electrodes, the phenomenon is less pronounced (Figures 2C,D and S6), but the increase in the R_{ct} values to 150 $\Omega\text{ cm}^2$ confirms the successful completion of the grafting step. This observation can be explained not only by a lower concentration of the grafted compounds but also by a different reactivity of the SLG layer toward the redox probe and/or to the charge transfer barrier induced by the grafted compound.^{40,72,73} After the deprotection step, the R_{ct} values decrease significantly close to the initial values of the bare electrodes, particularly for the FTO surfaces (Table 1). The recovery of the high conductivity properties of the surfaces is also visible in the voltammogram of the redox probe, which is almost identical to the one recorded for the unmodified electrode (Figure 2B,D). These results are in a good agreement with the formation of a monolayer³⁷ or a submonolayer and also indicate an interesting low barrier for the charge transfer between the modified electrode and the redox probe.⁴¹

The subsequent attachment of the NTA ligand by “click” chemistry is confirmed by the increase in the R_{ct} values between 130 and 220 $\Omega\text{ cm}^2$. As depicted in Figure 1, the Huisgen cycloaddition in the presence of a catalytic amount of

copper can result in the partial complexation of copper ions with the NTA-terminated wires. To overcome this issue, the complexed Cu^{2+} cations were removed by EDTA chelation, as confirmed from the EIS measurements showing a decrease in the R_{ct} values between 70 and 96 $\Omega\text{ cm}^2$. The higher R_{ct} for the complexed NTA could be explained by electrostatic interactions between the positively charged metal ion and the negatively charged FTO or FTO/SLG⁷⁴ surfaces, which results in a compact interface hindering the access to the redox probe. Conversely, after the EDTA treatment, the NTA moiety becomes negatively charged as it is devoid of metal cations, which induces electrostatic repulsion between the NTA moieties and the electrode surface, at the same time allowing for easier access to the redox probe.

The last step of metalation with the desired divalent cation M^{2+} (M^{2+} : Ni^{2+} or Co^{2+}) is demonstrated by the increase in R_{ct} values around 140 $\Omega\text{ cm}^2$ for FTO electrodes and around 115 $\Omega\text{ cm}^2$ for the FTO/SLG surfaces. Even though the absolute final values are different for both materials (Table 1), the calculation of the apparent fractional coverage θ ⁷⁵ confirms the homogeneous functionalization. Concerning the FTO surfaces, the apparent fractional coverage θ is calculated to be 0.67 and 0.74 for nickel- and cobalt-based architectures, respectively, while for the FTO/SLG samples, the corresponding values are 0.75 and 0.73, respectively.

Complementary to R_{ct} the evolution of the CPE parameters Q and Φ (Table S1) and the calculated double-layer capacitance C_{dl} (Table 1) provide additional information and confirm the homogeneity and high order of the metalorganic architecture. Although the low capacitance calculated for the bare FTO and FTO/SLG is representative of a non-capacitor behavior, a significant error in the fitted parameters should be kept in mind due to the measurements at high frequency, possibly affected by the porosity of the material. After the grafting step, all materials display a strong enhancement of the capacitance, which can be attributed to the entrapment of redox-inactive ions present in the electrolyte solution during electrografting. Interestingly, after the deprotection step, the capacitance values are relatively stable and the exponential factor Φ of the CPE element is closer to unity ($0.8 < \Phi < 0.93$), further confirming the formation of a well-organized and homogenous molecular interface.

Raman Spectroscopy Analyses. To further confirm the covalent grafting of the aryl diazonium salt on the substrates⁷⁶

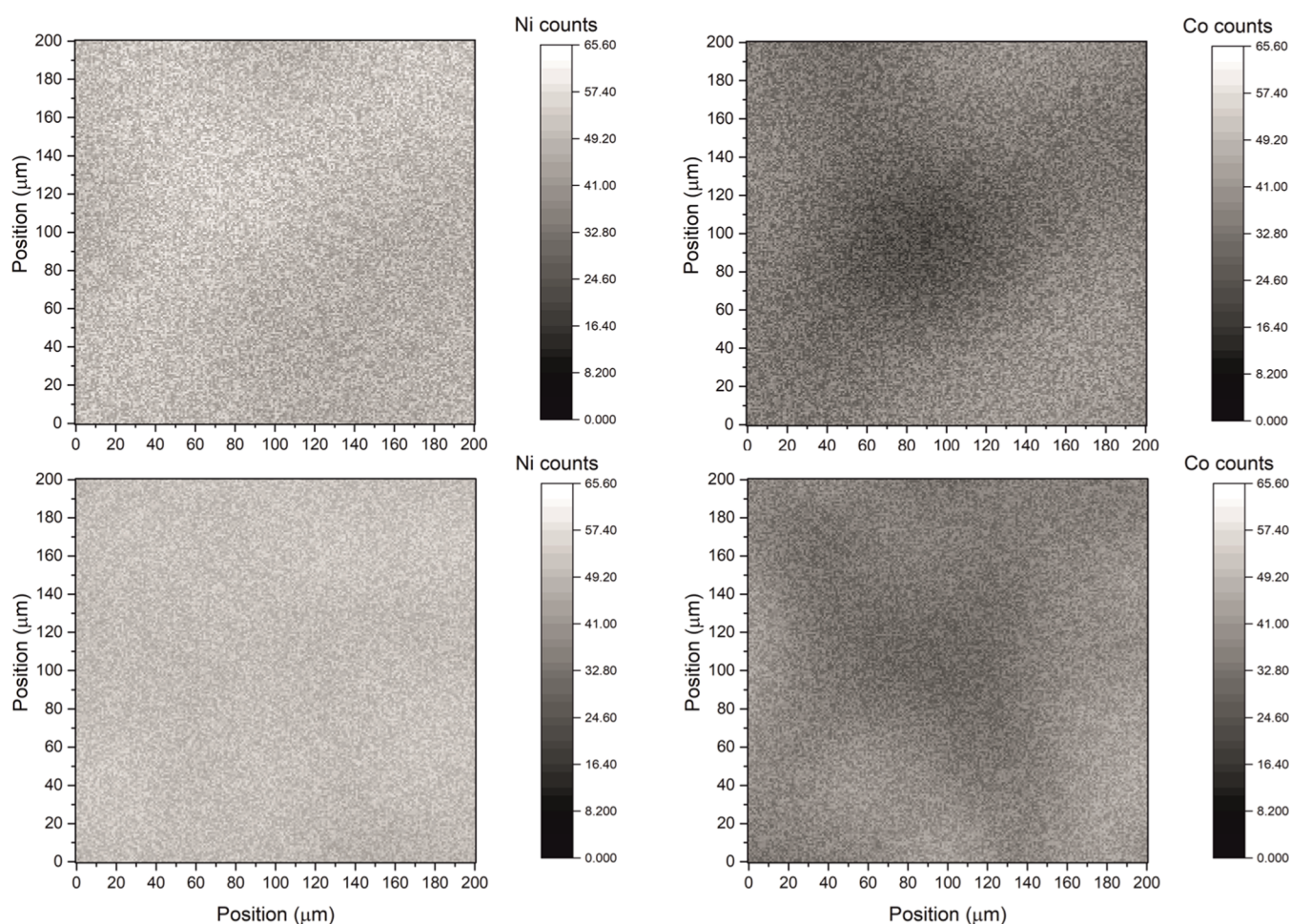


Figure 4. Atomic mapping by SIMS analysis of FTO-cNTA-M²⁺ electrodes with nickel (left) and cobalt (right) atoms after 1 h incubation (top) and overnight incubation (down) with the metal salt solutions.

and invalidate the hypothesis of solely physisorbed compounds, Raman spectroscopy analyses were performed on FTO/SLG before and after the grafting process and following the deprotection step (Figure S7). The pristine FTO/SLG presents the typical 2D and G signals at 2675.7 and 1583.0 cm⁻¹, respectively. The well-symmetrical and sharp shape of the 2D signal and a high I_{2D}/I_G ratio of 2.74 are characteristic of a high-quality graphene monolayer, and the low intensity of the D signal at 1342.8 cm⁻¹ reflects a small number of defects in the sp² lattice. After the covalent electrografting, the increase in the D intensity signal and the appearance of the D' signal at 1620.2 cm⁻¹ are typical of the creation of sp³ defects in the graphene honeycomb. Essentially, after the deprotection step, these features are preserved, and the I_D/I_G and I_{2D}/I_G ratios of 1.24 and 1.19, respectively, confirm the high coverage of covalently grafted aryl alkynes.

Finally, the homogeneity of the covalent functionalization was investigated in the entire system FTO/SLG-cNTA-Ni by Raman mapping, and the results are presented in the form of a correlation map (Figure 3A) with the representative Raman spectra at different correlation factors (Figure 3B). As illustrated in Figure 3, the correlation values range mainly from 0.6 to 1.0, indicating a substantial homogeneity of the functionalized surface, while the main difference between the spectra is relative to a slight variation in the D band intensity (1344.3 cm⁻¹).

SIMS Analysis. Previous studies in our group^{77,78} revealed that monolayers formed by different types of molecular wires terminated with cobalt and nickel-NTA complexes are not detectable by conventional CV on FTO or FTO/SLG surfaces when performed in an aqueous electrolyte. In order to obtain additional evidence about the presence of the different divalent cations at the molecular interface and gain a deeper insight into the metalation efficiency and homogeneity, secondary ions mass spectrometry (SIMS) analysis was performed on the covalently modified electrodes to detect the cobalt and nickel atoms (Figure 4). As the covalent wiring procedure and the efficiency of the functionalization process were shown to be similar for both types of electrode materials used in this study, the SIMS analysis was performed on FTO as this material is easier to manipulate for the reduced-size samples required for this experiment.

The obtained atomic mapping of the surfaces confirms the final step of metalation with cobalt and nickel. A highly homogenous and dense surface coverage has been achieved particularly for the Ni-containing samples (Figure 4, left). The efficient complexation between the NTA moiety and the nickel cation was obtained within 1 h of incubation with the cation and proceeded nearly quantitatively, and a longer incubation period does not affect the final surface coverage (Figure 4, left and down). Regarding cobalt ligation, a longer incubation time is required for the metalation step, as confirmed by SIMS (Figure 4, right). After 1 h of incubation, the SIMS analysis

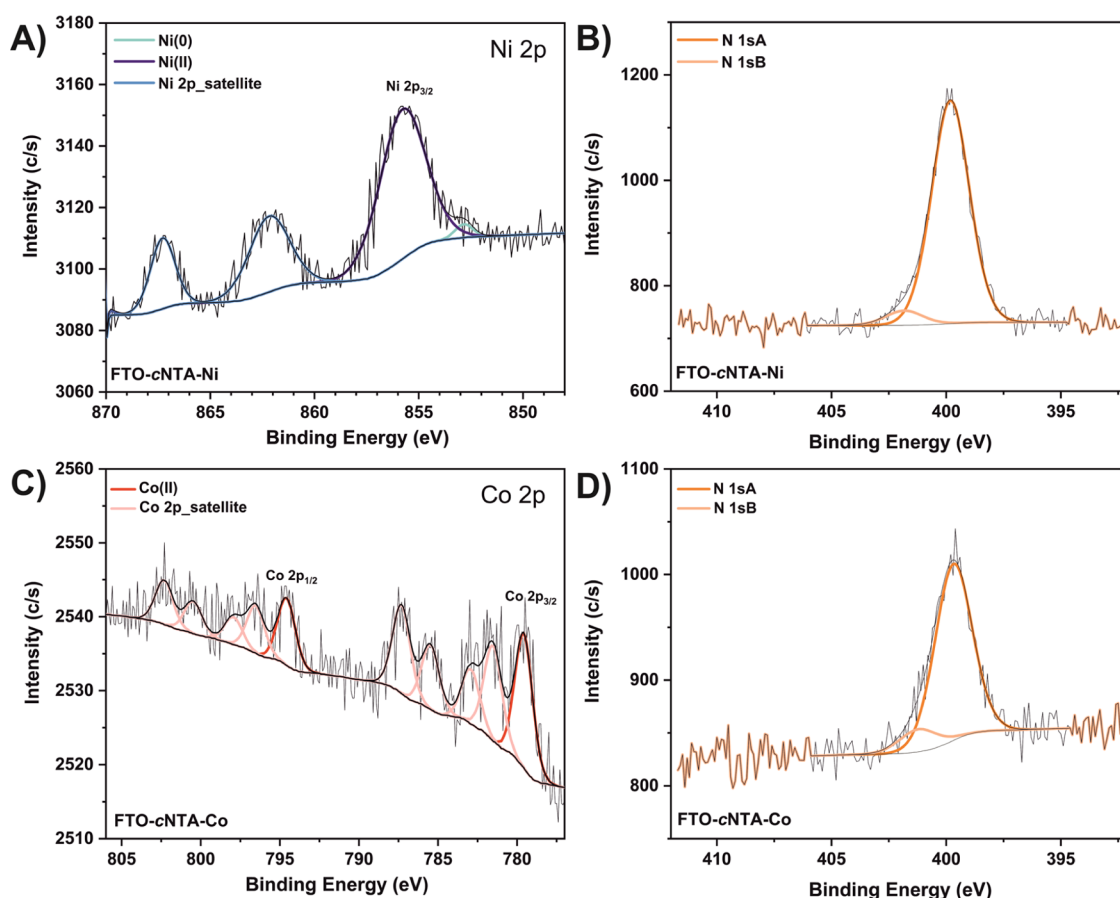


Figure 5. XPS of the FTO-cNTA-Ni²⁺ electrode (top) and FTO-cNTA-Co²⁺ electrode (bottom). (A) Region of the Ni 2p signals. (B) Region of the N 1s signals. (C) Region of the Co 2p signals. (D) Region of the N 1s signals.

revealed a noticeable heterogeneity of the surface, with the darker areas corresponding to a smaller concentration of cobalt cations. The final surface coverage density of cobalt was enhanced by overnight incubation, also resulting in a better surface homogeneity. These results were also confirmed by the EIS measurements, showing an increase in the resistance R_{ct} between the different incubation times for cobalt (data not shown).

XPS Analysis. After the optimization of the different functionalization steps, the elemental composition of the two metal-based wires grafted on FTO (FTO-cNTA-Ni and FTO-cNTA-Co) was dissected by XPS analysis. The most significant elements specific to the metalorganic wires were targeted, such as the nickel or cobalt cations and the nitrogen atoms (Figure 5). Similar to the SIMS analysis, the XPS measurements were performed on the reduced-size FTO surfaces only due to sample size constraints and easiness of manipulation of this material compared to FTO/SLG.

As shown in Figure 5, in addition to the signals derived from the substrate, the characteristic signals for the elements of interest were successfully detected for both metal-based functionalized FTO electrodes, confirming the complete construction of the molecular wires. For both the FTO-cNTA-Ni and FTO-cNTA-Co electrodes, the XPS analysis reveals a strong nitrogen signal compared to the control spectrum obtained for bare FTO (Figure S8). Interestingly, the different contributions of the nitrogen signal can be unambiguously assigned to the various nitrogen atoms present in the wire (Figure 5B,D). The prominent N 1sA signals

detected at 399.8 eV for FTO-cNTA-Ni and at 399.7 eV for FTO-cNTA-Co are compatible with the triazole bridge, while the smaller N 1sB signals recorded at 401.8 and 401.2 eV are attributed to the metalated nitrogen atom of the NTA moiety. Regarding the ligated metal cations (Figure 5A,C), the recorded signals confirmed the presence of nickel and cobalt and their respective +2 oxidation state. In the case of FTO-cNTA-Ni, the specific Ni(II) signal, Ni 2p_{3/2}, was detected at 855.8 eV and the Ni 2p satellites were detected at 862.3 and 867.5 eV. For FTO-cNTA-Co, the specific Co(II) signals, Co 2p_{3/2} and Co 2p_{1/2}, were detected respectively at 779.6 and 794.6 eV while their Co 2p satellites were obtained at 781.6, 782.9, 785.3, and 787.3 eV (Co 2p_{3/2}) and at 796.6, 797.9, 800.3 and 802.3 eV (Co 2p_{1/2}).

Photocurrent Generation. As mentioned above, the metal-NTA unit is commonly used as an anchoring group to immobilize His₆-tagged proteins. With the purpose of implementing *in fine* the highly active photo-enzymes, such as photosystem I (PSI)⁷⁹ in the wired SLG devices, the covalently functionalized electrodes were evaluated with respect to the photocurrent output. To this end, chronoamperometry measurements were performed at different potentials in an oxygenated aqueous buffer in the absence of any external mediators. The photocurrent density J values obtained within 30 s of the ON/OFF illumination period are presented in Figure 6 and summarized in Table 2.

Previous studies on the covalent grafting of diazonium salt on graphitic carbon nitride (g-C₃N₄) have shown a decrease in photocurrent generation with respect to the bare electrode

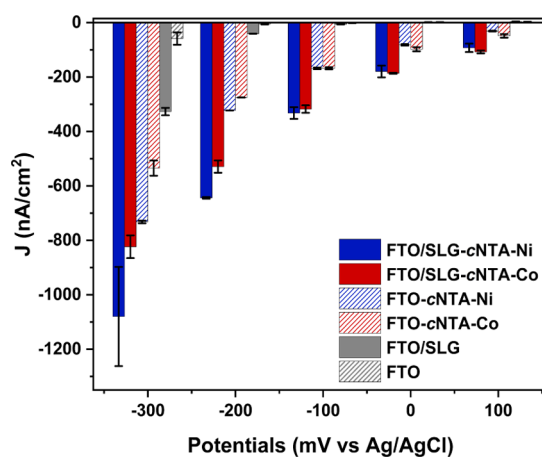


Figure 6. Photocurrent density generation of FTO and FTO/SLG electrodes at different applied potentials vs Ag/AgCl. The current density values correspond to the average values from two independent measurements with error bars representing standard deviation ($n = 2$).

material.^{80,81} In this study, all the covalently modified electrodes show a much higher photocurrent output compared to the control sample (bare FTO and FTO/SLG), confirming the great potential of the diazonium-derived wires, especially in the case of FTO/SLG electrodes (Figure 5). From -100 mV to the anodic region, both metal-based wires show roughly similar photocurrent output. At $+100$ mV, functionalized FTO electrodes generate around 13-fold higher current (~ 40 vs 3 nA/cm²) and approximately 25-fold higher current for the FTO/SLG electrodes (~ 100 vs 4 nA/cm²) compared to the control samples. At 0 mV, the FTO/SLG electrode shows the highest improvement (92-fold) in the photocurrent generation compared to the bare material (180 vs 2 nA/cm²), while the FTO electrodes have a 45-fold increase (~ 90 vs 2 nA/cm²). At -100 mV, a particularly high improvement is observed for the FTO electrodes with a 170-fold increase in photocurrent production compared to that of the bare material (170 vs 1 nA/cm²) and about 50-fold increase for the FTO/SLG surfaces (320 vs 6 nA/cm²). At -200 and -300 mV, the nickel-based nanoarchitectures yield higher photocurrent output compared to the cobalt counterparts. Although at -200 mV, the FTO and FTO/SLG electrodes showed an improvement of 50-fold and 14-fold, respectively, reaching values around 300 and 600 nA/cm², the highest photocurrent output was recorded for all the different architectures at -300 mV. Although the enhancement factor is smallest at -300 mV (10-fold and threefold for the FTO and FTO/SLG electrodes, respectively), the absolute photocurrent output values are the highest photocurrent densities recorded for any organic and

metalorganic wires on SLG reported to date (Table S2),^{79,82} in particular for the FTO/SLG-cNTA-Ni configuration, reaching an unprecedented value of $1 \mu\text{A}/\text{cm}^2$.

In addition to the high photocurrent output, the covalently modified electrode surface is characterized by the unidirectionality of the current produced. Indeed, in the anodic region, whereby both non-functionalized materials (FTO and FTO/SLG) generate a small anodic current at $+100$ mV, all the functionalized electrodes generate a strong cathodic photocurrent (Figures 7A and S9 and Table 2). It has already been shown that covalent grafting of SLG could greatly improve the conductivity of this material.⁵² Nevertheless, our study reveals for the first time the enhancement of photocurrent generation on FTO and FTO/SLG surfaces with a favored cathodic directionality (from the electrode to the wire). This is likely due to the introduction of a p-doping effect into the sp² lattice of SLG upon covalent grafting of the wires, leading to the modification of the electronic structure of the graphene monolayer, as shown for grafting with other types of diazonium salts.⁵⁰ A similar p-doping effect, which induces a unidirectional photocurrent output, was demonstrated for the graphitic C₃N₄ materials.⁸³

To verify the hypothesis of the existence of a p-doping effect, a Raman spectroscopy analysis was performed on the pristine FTO/SLG material and on the FTO/SLG-cNTA-Ni sample (Figure 7B). Indeed, Raman spectroscopy is a well-recognized approach not only to characterize graphene materials⁸⁴ in order to identify the quality of graphene, its intactness, and the number of deposited layers but also for the identification of the doping nature.^{85,86}

The representative Raman spectra (Figure 7B) show the typical features of the graphene monolayer and the induced changes after the covalent attachment of the full cNTA-Ni wire. For the pristine FTO/SLG sample, the characteristic 2D and G signals were detected at 2676.7 and 1587.3 cm⁻¹, respectively. The sharp and well-symmetrical shape of the 2D signal and a high I_{2D}/I_G ratio of 4.0 confirm the presence of a high-quality graphene monolayer. The minor D signal detected at 1343.4 cm⁻¹ and a low I_D/I_G ratio of 0.3 indicate the presence of a small number of defects in the graphene lattice. After covalent functionalization of SLG, a significant increase in the D signal is visible at 1344.3 cm⁻¹ together with the appearance of an additional D' signal at 1623.4 cm⁻¹. Both observations imply the introduction of the sp³-type defects in the graphene monolayer. An averaged calculated I_D/I_G ratio of 2.0 and an I_{2D}/I_G ratio of 1.88 indicate the high surface coverage with covalent wires. Importantly, after the covalent modification of SLG, the position of the 2D signal (ω_{2D}) is substantially blue-shifted from 3 to 10 cm⁻¹, confirming the p-doping effect^{85,86} induced by the cNTA-M wires.

Table 2. Photocurrent Density J Obtained for Functionalized FTO and FTO/SLG Electrodes at Different Applied Potentials vs Ag/AgCl in 5 mM Phosphate Buffer (pH 7)

samples	photocurrent density J (nA/cm ²)				
	+100 mV	0 mV	-100 mV	-200 mV	-300 mV
FTO	+3	+2	-1	-6	-59
FTO-cNTA-Ni	-31	-82	-168	-323	-733
FTO-cNTA-Co	-49	-98	-168	-275	-535
FTO/SLG	+4	+2	-6	-41	-327
FTO/SLG-cNTA-Ni	-93	-180	-332	-644	-1080
FTO/SLG-cNTA-Co	-108	-186	-318	-529	-824

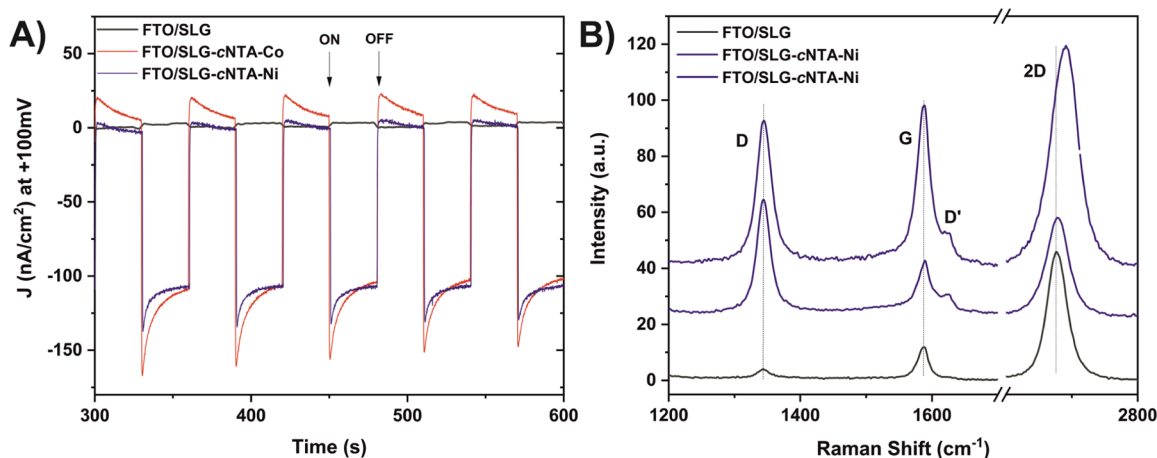


Figure 7. Photochronoamperometry of FTO (left) and FTO/SLG (right) electrodes at +100 mV vs Ag/AgCl in 5 mM phosphate buffer (pH 7). Representative Raman spectra ($\lambda_{\text{ex}} = 532$ nm) of pristine FTO/SLG and functionalized FTO/SLG-cNTA-Ni electrodes in two different areas.

Quantum Mechanical Analysis of the Electron Transfer Mechanism. The effect of different transition metal cations chelated with the NTA-terminated wires on the electronic properties of the SLG-SAM interfaces has been investigated by quantum mechanical (QM) modeling to assess the role of different metallic redox centers present within the wires in the direct electron transfer (DET) between the SLG and SAM of cNTA- M^{2+} . The QM calculation was conducted for three different transition metal ions (Ni^{2+} , Co^{2+} , and Cu^{2+}), all known to have high affinities to NTA and previously used in the bio-organic interface.^{77,79,87} In addition to the metal cations embedded into the organic interface of the electrodes (Co^{2+} and Ni^{2+}), in theoretical calculations of the electron transfer, we also used Cu^{2+} as a coordinated cation to computationally assess this potentially interesting system.

Work function shifts obtained for the interfaces with three different metal cations are presented in Table 3. We can clearly

Table 3. WF Shift Analysis for the Interfaces with Different Metal Coordination^a

	SLG-cNTA-Ni	SLG-cNTA-Co	SLG-cNTA-Cu
ΔWF (eV)	-0.57	-0.60	-0.01
ΔV_{SAM} (eV)	-1.46	-1.49	-1.00
BD (eV)	0.89	0.89	0.99
depolarization %	84	81	99
dipole (Debye)	2.00	2.09	0.02

^aDepolarization ratio is considered going from the isolated molecule to the fully formed interface.

see that the type of chelated cation strongly alters the ΔWF , with strong negative shifts of -0.57 and -0.60 eV for the SLG-cNTA-Ni and SLG-cNTA-Co interfaces, respectively, and a negligible shift of -10 meV for the SLG-cNTA-Cu interface. The observed negative shift in the WF for all the interfaces translates into the lowering of the electron injection barrier, which enhances the kinetics of DET. These results also show that the considered systems should display variable DET properties depending on the metal center used, which in turn leads to different electronic properties of the SLGs containing Ni^{2+} - or Co^{2+} -based covalently grafted wires. Moreover, these computational results are in full agreement with the electrochemical data under no external bias (Figure 6), whereas a slightly weaker current is measured for the SLG-cNTA-Ni

system, as compared to the SLG-cNTA-Co SAM (although it is worth mentioning that the smaller experimental value is within the error bars and the computationally obtained values are very close, likely within the expected accuracy of our approach).

To shed light on the different contributions of the total WF shift, we separately analyzed the two components of the shift, namely, the contribution arising from the molecular backbone (ΔV_{SAM} , i.e., the dipole moment along the molecular axis) and the contribution of the bond dipole (BD) arising from the chemisorption of the grafted SAM on graphene (i.e., the so-called supramolecular and pillow effect^{88,89}). The first contribution is relatively strong and has negative values for all the three SAMs of -1.46, -1.49, and -1.00 eV for the SLG-cNTA-Ni, SLG-cNTA-Co, and SLG-cNTA-Cu interfaces, respectively. On the other hand, the BD term is weaker and positive for all systems, with the values of 0.89 for both SLG-cNTA-Ni and SLG-cNTA-Co and 0.99 eV for SLG-cNTA-Cu (see Table 3). Interestingly, the BD contribution, defined as the contribution from the formation of the C-C bond between graphene and the SAM molecule, is not confined only to the SLG-SAM interface, but it evolves up to the end of the molecular backbone for all studied interfaces (Figure S10). As a result, for the Ni and Co interfaces, the ΔV_{SAM} and BD contributions counterbalance themselves to a certain degree, resulting in a total negative WF shift due to stronger ΔV_{SAM} contributions. On the other hand, for the Cu-containing nanoassembly, the two contributions virtually cancel out each other due to the strong charge recombination, leading to a negligible WF shift. This result suggests that the Cu-bearing system is not a good choice for this type of interface as experimentally it should translate to very low photocurrent densities and limited DET.

To rationalize the different contributions of the metal centers, we considered the changes in the molecular dipole moment of the SAM upon its immobilization on graphene. The value of the dipole moment component perpendicular to the graphene surface of isolated SAM molecules (considered in a large cell to avoid intermolecular interactions) was found to be 10.77, 10.72, and 4.25 Debye, for the NTA-Ni, NTA-Co, and NTA-Cu molecules, respectively. Depolarization effects strongly modify the molecular dipole moment when a densely packed interface is created, with the reduction of 84, 81, and 99% of their values, to obtain final dipole moments of 2.00,

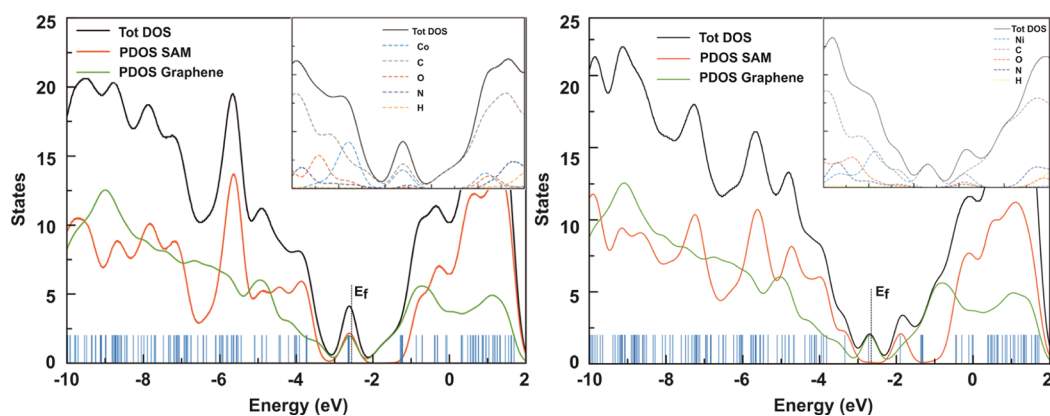


Figure 8. Total DOS and projected over the fragments and over each atom (insets) for the SLG-cNTA-Ni (left) and SLG-cNTA-Co (right) interfaces. The peaks corresponding to the highest occupied crystal orbital (HOCO) and lowest unoccupied crystal orbital (LUCO) levels are indicated. The vertical blue lines indicate the eigenvalues and the dotted line indicates the position of the Fermi energy level.

2.09, and 0.02 Debye for the SAM-NTA-Ni, SAM-NTA-Co, and SAM-NTA-Cu systems, respectively. The reason for the almost zero WF shift for the Cu-containing interface arises from both the strong depolarization and the strong charge recombination at the interface. Because the SLG-cNTA-Cu interface has been predicted to be not suitable for efficient DET, we will consider only the other two interfaces in the subsequent analyses.

Density of states (DOS) analysis has been performed to assess the nature of the DET at the different interfaces. Figure 8 shows the total DOS for the SLG-cNTA-M²⁺ interfaces and their projection on the two fragments of the system (SAM and graphene) and the projected DOS over each atom type. It is worth mentioning here that the presence of Ni²⁺ metal cations gives rise to a radical species, while the presence of Co²⁺ centers restores a “closed-shell” state. Thus, for the energy level analysis, we have to consider the states responsible for the valence band (VB), the mid-gap band responsible for the VB, the mid-gap band responsible for the soliton (SO), and the conduction band (CB) when Ni²⁺ is present, while only the VB and CB are considered for the Co²⁺-bearing system.

The presence of the Ni²⁺ metal center in SAM-cNTA-Ni shifts the energy of the frontier orbitals of the molecules closer to the Fermi energy of graphene, leading to a band gap opening of 0.83 eV. For this system, SO is pinned at the graphene Fermi level (−2.72 eV), while the VB is found at a much lower energy (−3.34 eV), suggesting that only the former can contribute to the DET arising from graphene, while the CB has a strong SAM contribution. At the same time, for the Co²⁺-containing system, we observe (a) two VB levels that are virtually degenerate at −2.62 eV and pinned at the graphene Fermi level with different orbital localization over different parts of the interface, which can both contribute to the electron transfer and (b) strong SAM localization for the CB (Figure 9). This, in turn, leads to a band gap opening of 1.76 eV, which is more than two times higher in comparison to the Ni²⁺ system. In addition, mid-gap states localized on graphene are present for both interfaces, in the −1.25 ± 0.05 eV (for SAM-cNTA-Co) and −1.30 ± 0.05 eV energy ranges (for SAM-cNTA-Ni). Interestingly, for the SAM-cNTA-Ni interface, these states are located at higher energy with respect to the LUCO, while the opposite is true for the SAM-cNTA-Co system, leading to substantial differences in the DET abilities.

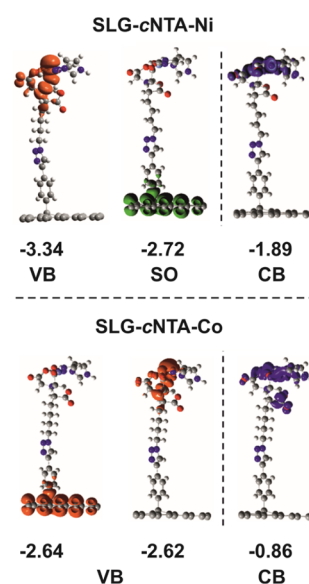


Figure 9. Frontier orbital analysis for the graphene-SAM-cNTA-Ni (top) and graphene-SAM-cNTA-Co (bottom) interfaces. Red color refers to the VB maximum (HOCO), green refers to the SO, and blue refers to the CB levels, respectively. The reported values refer to the energies associated to each orbital, in eV.

To understand the experimentally observed behavior of the interfaces, one should consider separately the experiments resulting in cathodic and anodic current directions for the two interfaces containing Co or Ni redox centers in the covalently grafted wires as they are likely governed by different mechanisms. When a cathodic external bias is applied, the DET occurs from graphene to the SAM. Although for SLG-cNTA-Ni, the DET occurs from the SO to the CB, for SLG-cNTA-Co, it involves the VB and the CB. This is possible due to the quasidegeneracy of the occupied frontier orbitals present at this interface (with the energy difference of less than 0.02 eV). On the other hand, when a strong negative bias is applied, a higher current is generated for the Ni²⁺-containing interface. This is the result of a relatively small gap opening of 0.83 eV, which facilitates the high current. On the other hand, a gap of 1.76 eV for the Co²⁺-containing system impedes the DET, resulting in a lower generated current.

When an anodic external bias is applied, a cathodic current is generated for both interfaces, with higher values for the SLG-

cNTA-Co one compared to those of SLG-cNTA-Ni. For the SLG-cNTA-Ni interface, the decrease in magnitude of the generated current is expected from our theoretical results because the external field counteracts the internal electron flow. On the other hand, for the Co²⁺-bearing interface, the presence of mid-gap states (localized on graphene) at lower energies compared to the LUCO is likely to be essential in enhancing the internal flow of charges, allowing for a stronger internal DET compared to the applied bias. In fact, the larger the band gap, the more difficult it is for electrons to be excited in the CB. Considering the substantial gap obtained for SLG-cNTA-Co, one might expect a lower DET from this interface, but due to the presence of gap states, the final DET may actually be enhanced. Furthermore, the negative generated current may also be a result of the ability of graphene (and, to a lesser extent, FTO) to act as a reservoir of mobile electrons that can be easily transferred to an accepting molecule, such as the SAM used in this study, upon the formation of a chemical bond.^{52,86} In fact, the presence of the sp³ degeneration leads to a shift of the Fermi energy level toward a more positive value, as confirmed by our theoretical modeling, leading to enhanced DET.

CONCLUSIONS

The covalent modification of FTO and FTO/SLG surfaces using the electrografting of diazonium salt derivatives was successfully demonstrated in this work. The crucial initial step to build a well-organized monolayer was achieved and optimized. The protection/deprotection strategy used for the construction of the full wire allows a further attachment of functionalities using the green approach of the “click” chemistry reaction. The Huisgen cycloaddition under mild aqueous conditions was used to immobilize the NTA ligand, whose metal complexes are commonly employed to attach a wide range of His₆-tagged proteins, including bio(photo)-electrocatalysts. The potential of the covalently grafted cNTA-M²⁺ wires bearing two different metal redox centers (cobalt and nickel) was demonstrated by the generation of photocurrents in an aqueous electrolyte, which occurred via DET (in the absence of external mediators). The photocurrent densities obtained for both FTO and FTO/SLG nanodevices showed exceptionally high output values, reaching more than 1 μA/cm² for the nickel-based wires on FTO/SLG. In addition to the significant photocurrent output, the study reveals a strong unidirectionality of the DET upon the covalent modification of SLG. Even when a positive bias is applied (+100 mV vs Ag/AgCl), the functionalized electrodes generate cathodic current in contrast to the bare FTO/SLG and FTO materials.

The observed photocurrent behavior implies that the covalently linked NTA-containing wires induce a strong p-doping effect in both electron-rich surfaces (FTO and FTO/SLG), which ultimately results in an enhanced unidirectional cathodic photocurrent generation. These results are rationalized by the QM modeling of the DET process between SLG and cNTA-M²⁺ SAM. Thus, the high DET obtained for the SLG-cNTA-Ni²⁺ system is due to a small band gap opening and localization of the frontier orbitals in different parts of the molecular interface (with occupied orbitals on SLG and virtual orbitals on the cNTA-Ni²⁺ SAM), favoring the cathodic current generation. On the other hand, the wide band gap detected for the SLG-cNTA-Co²⁺ system, together with the presence of mid-gap states localized on SLG, favors the enhancement of the cathodic current when a positive bias is applied.

Overall, our study paves the way for the development of highly efficient biohybrid photoactive nanodevices using a robust, universal, and highly conductive metalorganic interface for an array of applications, ranging from solar-to-fuel devices and biocatalytic nanosystems to biophotosensors, all of which require the high cathodic current output and minimized back reactions, both of which are essential for the maximization of solar conversion efficiency.

ASSOCIATED CONTENT

Supporting Information

The Supporting Information is available free of charge at <https://pubs.acs.org/doi/10.1021/acs.chemmater.2c00088>.

Additional experimental details, SLG characterizations, Nyquist plots and CVs of analyzed Co-based electrodes, complementary curve fitting parameters, additional Raman analyses, XPS analysis of FTO, photochromoamperometry of FTO-based electrodes at +100 mV, comparative photocurrent table, and QM result on the work function (PDF)

AUTHOR INFORMATION

Corresponding Authors

Margot Jacquet – Solar Fuels Laboratory, Centre of New Technologies, University of Warsaw, 02-097 Warsaw, Poland; Email: m.jacquet@cent.uw.edu.pl

Joanna Kargul – Solar Fuels Laboratory, Centre of New Technologies, University of Warsaw, 02-097 Warsaw, Poland; orcid.org/0000-0003-1410-1905; Email: j.kargul@cent.uw.edu.pl

Authors

Silvio Osella – Chemical and Biological Systems Simulation Lab, Centre of New Technologies, University of Warsaw, 02-097 Warsaw, Poland; orcid.org/0000-0001-8541-1914

Ersan Harputlu – Department of Engineering Fundamental Sciences, Faculty of Engineering, Tarsus University, 33400 Tarsus, Turkey

Barbara Palys – Faculty of Chemistry, University of Warsaw, 02-093 Warsaw, Poland; orcid.org/0000-0003-1113-2546

Monika Kaczmarek – Chemical and Biological Systems Simulation Lab, Centre of New Technologies, University of Warsaw, 02-097 Warsaw, Poland

Ewa K. Nawrocka – Laboratory of NMR Spectroscopy, Centre of New Technologies, University of Warsaw, 02-097 Warsaw, Poland; orcid.org/0000-0002-4801-7894

Adam A. Rajkiewicz – Laboratory of Chemical Synthesis Methodology, Centre of New Technologies, University of Warsaw, 02-097 Warsaw, Poland

Marcin Kalek – Laboratory of Chemical Synthesis Methodology, Centre of New Technologies, University of Warsaw, 02-097 Warsaw, Poland; orcid.org/0000-0002-1595-9818

Paweł P. Michałowski – Łukasiewicz Research Network—Institute of Microelectronics and Photonics, 02-668 Warsaw, Poland; orcid.org/0000-0002-3299-4092

Bartosz Trzaskowski – Chemical and Biological Systems Simulation Lab, Centre of New Technologies, University of Warsaw, 02-097 Warsaw, Poland

C. Gokhan Unlu – Department of Biomedical Engineering, Pamukkale University, TR-20070 Denizli, Turkey

Wojciech Lisowski – Institute of Physical Chemistry, Polish Academy of Science, 01-224 Warsaw, Poland

Marcin Pisarek – Institute of Physical Chemistry, Polish Academy of Science, 01-224 Warsaw, Poland; orcid.org/0000-0002-7424-5954

Krzysztof Kazmierczuk – Laboratory of NMR Spectroscopy, Centre of New Technologies, University of Warsaw, 02-097 Warsaw, Poland; orcid.org/0000-0001-9585-1737

Kasim Ocakoglu – Department of Engineering Fundamental Sciences, Faculty of Engineering, Tarsus University, 33400 Tarsus, Turkey

Agnieszka Więckowska – Faculty of Chemistry, University of Warsaw, 02-093 Warsaw, Poland

Complete contact information is available at:

<https://pubs.acs.org/10.1021/acs.chemmater.2c00088>

Author Contributions

M.J.: conceptualization, investigation, formal analysis, methodology, project administration, validation, visualization, and writing—original draft. S.O. and M.K.: formal analysis and writing—original draft. B.P., E.N., P.M., W.L., M.P.: investigation. E.H., A.A.R., M.K., C.G.U., and K.O.: resources and writing—review and editing. B.T., K.K., and A.W.: writing—review and editing. J.K.: conceptualization, funding acquisition, project administration, supervision, and writing—review and editing.

Notes

The authors declare no competing financial interest.

ACKNOWLEDGMENTS

M.J. and J.K. acknowledge the financial support from the Polish National Science Centre (OPUS14 grant no. UMO-2017/27/B/ST5/00472 to J.K.). S.O. acknowledges the financial support from the Polish National Science Centre (SONATA14 grant no. UMO-2018/31/D/ST4/01475). Computational resources were provided by the Interdisciplinary Centre for Mathematical and Computational Modeling (ICM, University of Warsaw) under the G83-28 computational grant. We are grateful to Prof. Rafał Jurczakowski (CNBCh UW & Faculty of Chemistry, University of Warsaw, Poland) for his insightful comments on the article and Mateusz Kasztelan (CNBCh UW and Faculty of Chemistry, University of Warsaw, Poland) for his assistance with the Raman spectroscopy measurements.

REFERENCES

- (1) Sachan, P.; Mondal, P. C. Versatile Electrochemical Approaches towards the Fabrication of Molecular Electronic Devices. *Analyst* **2020**, *145*, 1563–1582.
- (2) Qi, M.; Zhang, Y.; Cao, C.; Lu, Y.; Liu, G. Increased Sensitivity of Extracellular Glucose Monitoring Based on AuNP Decorated GO Nanocomposites. *RSC Adv.* **2016**, *6*, 39180–39187.
- (3) Harris, T. G. A. A.; Heidary, N.; Kozuch, J.; Frielingsdorf, S.; Lenz, O.; Mroginski, M.-A.; Hildebrandt, P.; Zebger, I.; Fischer, A. In Situ Spectroelectrochemical Studies into the Formation and Stability of Robust Diazonium-Derived Interfaces on Gold Electrodes for the Immobilization of an Oxygen-Tolerant Hydrogenase. *ACS Appl. Mater. Interfaces* **2018**, *10*, 23380–23391.
- (4) Bangle, R.; Sampaio, R. N.; Troian-Gautier, L.; Meyer, G. J. Surface Grafting of Ru(II) Diazonium-Based Sensitizers on Metal Oxides Enhances Alkaline Stability for Solar Energy Conversion. *ACS Appl. Mater. Interfaces* **2018**, *10*, 3121–3132.
- (5) Tarpani, L.; Bellezza, F.; Sassi, P.; Gambucci, M.; Cipiciani, A.; Latterini, L. New Insights into the Effects of Surface Functionalization

on the Peroxidase Activity of Cytochrome c Adsorbed on Silica Nanoparticles. *J. Phys. Chem. B* **2019**, *123*, 2567–2575.

(6) Charlton, M. R.; Suhr, K. J.; Holliday, B. J.; Stevenson, K. J. Electrochemical Modification of Indium Tin Oxide Using Di(4-Nitrophenyl) Iodonium Tetrafluoroborate. *Langmuir* **2015**, *31*, 695–702.

(7) Friebe, V. M.; Millo, D.; Swainsbury, D. J. K.; Jones, M. R.; Frese, R. N. Cytochrome c Provides an Electron-Funneling Antenna for Efficient Photocurrent Generation in a Reaction Center Biophotocathode. *ACS Appl. Mater. Interfaces* **2017**, *9*, 23379–23388.

(8) Hirsch, A.; Englert, J. M.; Hauke, F. Wet Chemical Functionalization of Graphene. *Acc. Chem. Res.* **2013**, *46*, 87–96.

(9) Furmansky, Y.; Sergani, S.; Ashkenasy, N.; Visoly-Fisher, I. Photoconductance of ITO/Conductive Polymer Junctions in the UV and Visible Ranges. *J. Phys. Chem. C* **2018**, *122*, 7288–7295.

(10) Schmid, E. L.; Keller, T. A.; Dienes, Z.; Vogel, H. Reversible Oriented Surface Immobilization of Functional Proteins on Oxide Surfaces. *Anal. Chem.* **1997**, *69*, 1979–1985.

(11) Hu, P.; Gao, S.; Zhang, Y.; Zhang, L.; Wang, C. Surface Modified BaTiO₃ Nanoparticles by Titanate Coupling Agent Induce Significantly Enhanced Breakdown Strength and Larger Energy Density in PVDF Nanocomposite. *Compos. Sci. Technol.* **2018**, *156*, 109–116.

(12) Hotchkiss, P. J.; Jones, S. C.; Paniagua, S. A.; Sharma, A.; Kippelen, B.; Armstrong, N. R.; Marder, S. R. The Modification of Indium Tin Oxide with Phosphonic Acids: Mechanism of Binding, Tuning of Surface Properties, and Potential for Use in Organic Electronic Applications. *Acc. Chem. Res.* **2012**, *45*, 337–346.

(13) Tuccitto, N.; Giambianco, N.; Licciardello, A.; Marletta, G. Patterning of Lactoferrin Using Functional SAMs of Iron Complexes. *Chem. Commun.* **2007**, 2621–2623.

(14) Delamar, M.; Hitmi, R.; Pinson, J.; Savéant, J. M. Covalent Modification of Carbon Surfaces by Grafting of Functionalized Aryl Radicals Produced from Electrochemical Reduction of Diazonium Salts. *J. Am. Chem. Soc.* **1992**, *114*, 5883–5884.

(15) Hetemi, D.; Noël, V.; Pinson, J. Grafting of Diazonium Salts on Surfaces: Application to Biosensors. *Biosensors* **2020**, *10*, 1–32.

(16) Sandomierski, M.; Voelkel, A. Diazonium Modification of Inorganic and Organic Fillers for the Design of Robust Composites: A Review. *J. Inorg. Organomet. Polym. Mater.* **2021**, *31*, 1–21.

(17) Stewart, M. P.; Maya, F.; Kosynkin, D. V.; Dirk, S. M.; Stapleton, J. J.; McGuinness, C. L.; Allara, D. L.; Tour, J. M. Direct Covalent Grafting of Conjugated Molecules onto Si, GaAs, and Pd Surfaces from Aryldiazonium Salts. *J. Am. Chem. Soc.* **2004**, *126*, 370–378.

(18) Busson, M.; Berisha, A.; Combellas, C.; Kanoufi, F.; Pinson, J. Photochemical Grafting of Diazonium Salts on Metals. *Chem. Commun.* **2011**, *47*, 12631–12633.

(19) Drevet, R.; Dragoé, D.; Barthés-Labrousse, M. G.; Chaussé, A.; Andrieux, M. XPS-Nanocharacterization of Organic Layers Electrochemically Grafted on the Surface of SnO₂ Thin Films to Produce a New Hybrid Material Coating. *Appl. Surf. Sci.* **2016**, *384*, 442–448.

(20) Wang, C.; Huang, N.; Zhuang, H.; Jiang, X. Enhanced Performance of Nanocrystalline ZnO DNA Biosensor via Introducing Electrochemical Covalent Biolinkers. *ACS Appl. Mater. Interfaces* **2015**, *7*, 7605–7612.

(21) Lamberti, F.; Agnoli, S.; Brigo, L.; Granozzi, G.; Giomo, M.; Elvassore, N. Surface Functionalization of Fluorine-Doped Tin Oxide Samples through Electrochemical Grafting. *ACS Appl. Mater. Interfaces* **2013**, *5*, 12887–12894.

(22) Maldonado, S.; Smith, T. J.; Williams, R. D.; Morin, S.; Barton, E.; Stevenson, K. J. Surface Modification of Indium Tin Oxide via Electrochemical Reduction of Aryldiazonium Cations. *Langmuir* **2006**, *22*, 2884–2891.

(23) Combellas, C.; Kanoufi, F.; Pinson, J.; Podvorica, F. I. Sterically Hindered Diazonium Salts for the Grafting of a Monolayer on Metals. *J. Am. Chem. Soc.* **2008**, *130*, 8576–8577.

(24) Raicopol, M. D.; Andronescu, C.; Atasiei, R.; Hanganu, A.; Vasile, E.; Brezoiu, A. M.; Pilan, L. Organic Layers via Aryl Diazonium

Electrochemistry: Towards Modifying Platinum Electrodes for Interference Free Glucose Biosensors. *Electrochim. Acta* **2016**, *206*, 226–237.

(25) Combellas, C.; Delamar, M.; Kanoufi, F.; Pinson, J.; Podvorica, F. I. Spontaneous Grafting of Iron Surfaces by Reduction of Aryldiazonium Salts in Acidic or Neutral Aqueous Solution. Application to the Protection of Iron against Corrosion. *Chem. Mater.* **2005**, *17*, 3968–3975.

(26) Cottineau, T.; Morin, M.; Bélanger, D. Surface Band Structure of Aryl-Diazonium Modified p-Si Electrodes Determined by X-Ray Photoelectron Spectroscopy and Electrochemical Measurements. *RSC Adv.* **2013**, *3*, 23649–23657.

(27) Picot, M.; Lapinsonnière, L.; Rothbaler, M.; Barrière, F. Graphite Anode Surface Modification with Controlled Reduction of Specific Aryl Diazonium Salts for Improved Microbial Fuel Cells Power Output. *Sensens. Bioelectron.* **2011**, *28*, 181–188.

(28) Allongue, P.; Delamar, M.; Desbat, B.; Fagebaume, O.; Hitmi, R.; Pinson, J.; Savéant, J.-M. Covalent Modification of Carbon Surfaces by Aryl Radicals Generated from the Electrochemical Reduction of Diazonium Salts. *J. Am. Chem. Soc.* **1997**, *119*, 201–207.

(29) Stockhausen, V.; Ghilane, J.; Martin, P.; Trippé-Allard, G.; Randriamahazaka, H.; Lacroix, J.-C. Grafting Oligothiophenes on Surfaces by Diazonium Electroreduction: A Step toward Ultrathin Junction with Well-Defined Metal/Oligomer Interface. *J. Am. Chem. Soc.* **2009**, *131*, 14920–14927.

(30) Li, H.; Cheng, F.; Duft, A. M.; Adronov, A. Functionalization of Single-Walled Carbon Nanotubes with Well-Defined Polystyrene by “Click” Coupling. *J. Am. Chem. Soc.* **2005**, *127*, 14518–14524.

(31) Kirkman, P. M.; Güell, A. G.; Cuharuc, A. S.; Unwin, P. R. Spatial and Temporal Control of the Diazonium Modification of Sp² Carbon Surfaces. *J. Am. Chem. Soc.* **2014**, *136*, 36–39.

(32) Paulus, G. L. C.; Wang, Q. H.; Strano, M. S. Covalent Electron Transfer Chemistry of Graphene with Diazonium Salts. *Acc. Chem. Res.* **2013**, *46*, 160–170.

(33) Raymakers, J.; Artemenko, A.; Verstraeten, F.; Krysova, H.; Cermák, J.; Nicley, S. S.; Lopez-Carballeira, D.; Kromka, A.; Haenen, K.; Kavan, L.; Maes, W.; Rezek, B. Photogenerated Charge Collection on Diamond Electrodes with Covalently Linked Chromophore Monolayers. *Electrochim. Acta* **2020**, *337*, 135762.

(34) Harris, T. G. A. A.; Götz, R.; Wrzolek, P.; Davis, V.; Knapp, C. E.; Ly, K.; Hildebrandt, P.; Schwalbe, M.; Weidinger, I.; Zebger, I.; Fischer, A. Robust Electrografted Interfaces on Metal Oxides for Electrocatalysis—an in Situ Spectroelectrochemical Study. *J. Mater. Chem. A* **2018**, *6*, 15200–15212.

(35) de Villeneuve, C. H.; Pinson, J.; Bernard, M. C.; Allongue, P. Electrochemical Formation of Close-Packed Phenyl Layers on Si(111). *J. Phys. Chem. B* **1997**, *101*, 2415–2420.

(36) Schirowski, M.; Hauke, F.; Hirsch, A. Controlling the Degree of Functionalization: In-Depth Quantification and Side-Product Analysis of Diazonium Chemistry on SWCNTs. *Chem.—Eur. J.* **2019**, *25*, 12761–12768.

(37) D'Amours, M.; Bélanger, D. Stability of Substituted Phenyl Groups Electrochemically Grafted at Carbon Electrode Surface. *J. Phys. Chem. B* **2003**, *107*, 4811–4817.

(38) Mahouche-Chergui, S.; Gam-Derouich, S.; Mangeney, C.; Chehimi, M. M. Aryl Diazonium Salts: A New Class of Coupling Agents for Bonding Polymers, Biomacromolecules and Nanoparticles to Surfaces. *Chem. Soc. Rev.* **2011**, *40*, 4143–4166.

(39) Pinson, J.; Podvorica, F. Attachment of Organic Layers to Conductive or Semiconductive Surfaces by Reduction of Diazonium Salts. *Chem. Soc. Rev.* **2005**, *34*, 429–439.

(40) Leroux, Y. R.; Hapiot, P. Nanostructured Monolayers on Carbon Substrates Prepared by Electrografting of Protected Aryldiazonium Salts. *Chem. Mater.* **2013**, *25*, 489–495.

(41) Leroux, Y. R.; Fei, H.; Noël, J.-M.; Roux, C.; Hapiot, P. Efficient Covalent Modification of a Carbon Surface: Use of a Silyl Protecting Group to Form an Active Monolayer. *J. Am. Chem. Soc.* **2010**, *132*, 14039–14041.

(42) Liu, W.; Tilley, T. D. Sterically Controlled Functionalization of Carbon Surfaces With-6H₄CH₂X (X = OSO₂Me or N₃) Groups for Surface Attachment of Redox-Active Molecules. *Langmuir* **2015**, *31*, 1189–1195.

(43) Benson, M. C.; Ruther, R. E.; Gerken, J. B.; Rigsby, M. L.; Bishop, L. M.; Tan, Y.; Stahl, S. S.; Hamers, R. J. Modular “Click” Chemistry for Electrochemically and Photoelectrochemically Active Molecular Interfaces to Tin Oxide Surfaces. *ACS Appl. Mater. Interfaces* **2011**, *3*, 3110–3119.

(44) Yáñez-Sedeño, P.; González-Cortés, A.; Campuzano, S.; Pingarrón, J. M. Copper(I)-Catalyzed Click Chemistry as a Tool for the Functionalization of Nanomaterials and the Preparation of Electrochemical (Bio)Sensors. *Sensors* **2019**, *19*, 2379.

(45) Zhu, Y.; Murali, S.; Cai, W.; Li, X.; Suk, J. W.; Potts, J. R.; Ruoff, R. S. Graphene and Graphene Oxide: Synthesis, Properties, and Applications. *Adv. Mater.* **2010**, *22*, 3906–3924.

(46) Perreault, F.; Fonseca De Faria, A.; Elimelech, M. Environmental Applications of Graphene-Based Nanomaterials. *Chem. Soc. Rev.* **2015**, *44*, 5861–5896.

(47) Peña-Bahamonde, J.; Nguyen, H. N.; Fanourakis, S. K.; Rodrigues, D. F. Recent Advances in Graphene-Based Biosensor Technology with Applications in Life Sciences. *J. Nanobiotechnol.* **2018**, *16*, 75.

(48) Carvalho, A. F.; Kulyk, B.; Fernandes, A. J. S.; Fortunato, E.; Costa, F. M. A Review on the Applications of Graphene in Mechanical Transduction. *Adv. Mater.* **2021**, *34*, 2101326.

(49) Zhang, H.; Bekyarova, E.; Huang, J.-W.; Zhao, Z.; Bao, W.; Wang, F.; Haddon, R. C.; Lau, C. N. Aryl Functionalization as a Route to Band Gap Engineering in Single Layer Graphene Devices. *Nano Lett.* **2011**, *11*, 4047–4051.

(50) Farmer, D. B.; Golizadeh-Mojarad, R.; Perebeinos, V.; Lin, Y.-M.; Tulevski, G. S.; Tsang, J. C.; Avouris, P. Chemical Doping and Electron-Hole Conduction Asymmetry in Graphene Devices. *Nano Lett.* **2009**, *9*, 388–392.

(51) Hong, J.; Niyogi, S.; Bekyarova, E.; Itkis, M. E.; Ramesh, P.; Amos, N.; Litvinov, D.; Berger, C.; De Heer, W. A.; Khizroev, S.; Haddon, R. C. Effect of Nitrophenyl Functionalization on the Magnetic Properties of Epitaxial Graphene. *Small* **2011**, *7*, 1175–1180.

(52) Huang, P.; Zhu, H.; Jing, L.; Zhao, Y.; Gao, X. Graphene Covalently Binding Aryl Groups: Conductivity Increases Rather than Decreases. *ACS Nano* **2011**, *5*, 7945–7949.

(53) Fischer, N.; Goddard-Borger, E. D.; Greiner, R.; Klapötke, T. M.; Skelton, B. W.; Stierstorfer, J. Sensitivities of Some Imidazole-1-Sulfonyl Azide Salts. *J. Org. Chem.* **2012**, *77*, 1760–1764.

(54) Hwang, J.-J.; Tour, J. M. Combinatorial Synthesis of Oligo(Phenylene Ethynylene) S. *Tetrahedron* **2002**, *58*, 10387–10405.

(55) Lascaux, A.; Delahousse, G.; Ghostin, J.; Bouillon, J.-P.; Jabin, I. Second Generation Calix[6]Trenamides-Highly Selective Graftable Receptors for Neutral Guests and Contact Ion Pairs. *Eur. J. Org. Chem.* **2011**, 5272–5278.

(56) Porezag, D.; Frauenheim, T.; Köhler, T.; Seifert, G.; Kaschner, R. Construction of Tight-Binding-like Potentials on the Basis of Density-Functional Theory: Application to Carbon. *Phys. Rev. B: Condens. Matter Mater. Phys.* **1995**, *51*, 12947–12957.

(57) Osella, S.; Kiliszek, M.; Harputlu, E.; Unlu, C. G.; Ocakoglu, K.; Kargul, J.; Trzaskowski, B. Controlling the Charge Transfer Flow at the Graphene/Pyrene-Nitrotriacetic Acid Interface. *J. Mater. Chem. C* **2018**, *6*, 5046–5054.

(58) Osella, S.; Kiliszek, M.; Harputlu, E.; Unlu, C. G.; Ocakoglu, K.; Trzaskowski, B.; Kargul, J. Role of Metal Centers in Tuning the Electronic Properties of Graphene-Based Conductive Interfaces. *J. Phys. Chem. C* **2019**, *123*, 8623–8632.

(59) Aradi, B.; Hourahine, B.; Frauenheim, T. DFTB+, a Sparse Matrix-Based Implementation of the DFTB Method. *J. Phys. Chem. A* **2007**, *111*, 5678–5684.

(60) Giannozzi, P.; Baroni, S.; Bonini, N.; Calandra, M.; Car, R.; Cavazzoni, C.; Ceresoli, D.; Chiarotti, G. L.; Cococcioni, M.; Dabo, I.; Dal Corso, A.; De Gironcoli, S.; Fabris, S.; Fratesi, G.; Gebauer, R.

- Gerstmann, U.; Gougoussis, C.; Kokalj, A.; Lazzeri, M.; Martin-Samos, L.; Marzari, N.; Mauri, F.; Mazzarello, R.; Paolini, S.; Pasquarello, A.; Paulatto, L.; Sbraccia, C.; Scandolo, S.; Sclauzero, G.; Seitsonen, A. P.; Smogunov, A.; Umari, P.; Wentzcovitch, R. M. QUANTUM ESPRESSO: A Modular and Open-Source Software Project for Quantum Simulations of Materials. *J. Phys.: Condens. Matter* **2009**, *21*, 395502.
- (61) Perdew, J. P.; Burke, K.; Ernzerhof, M. Generalized Gradient Approximation Made Simple. *Phys. Rev. Lett.* **1996**, *77*, 3865–3868.
- (62) Perdew, J. P.; Burke, K.; Ernzerhof, M. Generalized Gradient Approximation Made Simple (Vol 77, Pg 3865, 1996). *Phys. Rev. Lett.* **1997**, *78*, 1396.
- (63) Vanderbilt, D. Soft Self-Consistent Pseudopotentials in a Generalized Eigenvalue Formalism. *Phys. Rev. B: Condens. Matter Mater. Phys.* **1990**, *41*, 7892–7895.
- (64) Evans, S. D.; Urankar, E.; Ulman, A.; Ferris, N. Self-Assembled Monolayers of Alkanethiols Containing a Polar Aromatic Group: Effects of the Dipole Position on Molecular Packing, Orientation, and Surface Wetting Properties. *J. Am. Chem. Soc.* **1991**, *113*, 4121–4131.
- (65) Zehner, R. W.; Parsons, B. F.; Hsung, R. P.; Sita, L. R. Tuning the Work Function of Gold with Self-Assembled Monolayers Derived from X - [C 6 H 4 - C t C -] n C 6 H 4 - SH (n) 0 , 1 , 2 ; X) H , F , CH 3 , CF 3 , and OCH 3). *Langmuir* **1999**, *15*, 1121–1127.
- (66) Chen, C.-Y.; Wu, K.-Y.; Chao, Y.-C.; Zan, H.-W.; Meng, H.-F.; Tao, Y.-T. Concomitant Tuning of Metal Work Function and Wetting Property with Mixed Self-Assembled Monolayers. *Org. Electron.* **2011**, *12*, 148–153.
- (67) Heimel, G.; Salzmann, I.; Duhm, S.; Koch, N. Design of Organic Semiconductors from Molecular Electrostatics. *Chem. Mater.* **2011**, *23*, 359–377.
- (68) Cahen, D.; Kahn, A. Electron Energetics at Surfaces and Interfaces: Concepts and Experiments. *Adv. Mater.* **2003**, *15*, 271–277.
- (69) Yang, Y.; Ibrahim, A. A.; Stockdill, J. L.; Hashemi, P. A Density-Controlled Scaffolding Strategy for Covalent Functionalization of Carbon-Fiber Microelectrodes. *Anal. Methods* **2015**, *7*, 7352–7357.
- (70) Blankespoor, R.; Limoges, B.; Schöllhorn, B.; Syssa-Magalé, J.-L.; Yazidi, D. Dense Monolayers of Metal-Chelating Ligands Covalently Attached to Carbon Electrodes Electrochemically and Their Useful Application in Affinity Binding of Histidine-Tagged Proteins. *Langmuir* **2005**, *21*, 3362–3375.
- (71) Hirschorn, B.; Orazem, M. E.; Tribollet, B.; Vivier, V.; Frateur, I.; Musiani, M. Determination of Effective Capacitance and Film Thickness from Constant-Phase-Element Parameters. *Electrochim. Acta* **2010**, *55*, 6218–6227.
- (72) Chen, P.; Fryling, M. A.; McCreery, R. L. Electron Transfer Kinetics at Modified Carbon Electrode Surfaces: The Role of Specific Surface Site. *Anal. Chem.* **1995**, *67*, 3115–3122.
- (73) Chen, P.; McCreery, R. L. Control of Electron Transfer Kinetics at Glassy Carbon Electrodes by Specific Surface Modification. *Anal. Chem.* **1996**, *68*, 3958–3965.
- (74) Bepete, G.; Anglaret, E.; Ortolani, L.; Morandi, V.; Huang, K.; Pénicaut, A.; Drummond, C. Surfactant-Free Single-Layer Graphene in Water. *Nat. Chem.* **2017**, *9*, 347–352.
- (75) Janek, R. P.; Fawcett, W. R.; Ulman, A. Impedance Spectroscopy of Self-Assembled Monolayers on Au(111): Sodium Ferrocyanide Charge Transfer at Modified Electrodes. *Langmuir* **1998**, *14*, 3011–3018.
- (76) Xia, Z.; Leonardi, F.; Gobbi, M.; Liu, Y.; Bellani, V.; Liscio, A.; Kovtun, A.; Li, R.; Feng, X.; Orgiu, E.; Samori, P.; Treossi, E.; Palermo, V. Electrochemical Functionalization of Graphene at the Nanoscale with Self-Assembling Diazonium Salts. *ACS Nano* **2016**, *10*, 7125–7134.
- (77) Jacquet, M.; Kiliszek, M.; Osella, S.; Izzo, M.; Sar, J.; Harputlu, E.; Unlu, C. G.; Trzaskowski, B.; Ocakoglu, K.; Kargul, J. Molecular Mechanism of Direct Electron Transfer in the Robust Cytochrome-Functionalised Graphene Nanosystem. *RSC Adv.* **2021**, *11*, 18860–18869.
- (78) Izzo, M.; Osella, S.; Jacquet, M.; Kiliszek, M.; Harputlu, E.; Starkowska, A.; Łasica, A.; Unlu, C. G.; Uspiński, T.; Niewiadomski, P.; Bartosik, D.; Trzaskowski, B.; Ocakoglu, K.; Kargul, J. Enhancement of Direct Electron Transfer in Graphene Bioelectrodes Containing Novel Cytochrome C553 Variants with Optimized Heme Orientation. *Bioelectrochemistry* **2021**, *140*, 107818.
- (79) Kiliszek, M.; Harputlu, E.; Szalkowski, M.; Kowalska, D.; Unlu, C. G.; Haniewicz, P.; Abram, M.; Wiwatowski, K.; Niedziółka-Jönsson, J.; Maćkowski, S.; Ocakoglu, K.; Kargul, J. Orientation of Photosystem i on Graphene through Cytochrome: C 553 Leads to Improvement in Photocurrent Generation. *J. Mater. Chem. A* **2018**, *6*, 18615–18626.
- (80) Gao, Z.; Chen, K.; Wang, L.; Bai, B.; Liu, H.; Wang, Q. Aminated Flower-like ZnIn2S4 Coupled with Benzoic Acid Modified g-C3N4 Nanosheets via Covalent Bonds for Ameliorated Photocatalytic Hydrogen Generation. *Appl. Catal., B* **2020**, *268*, 118462.
- (81) Huang, M.; Tian, J.; Zhou, C.; Bai, P.; Lu, J. Photoelectrochemical Determination for Acid Phosphatase Activity Based on an Electron Inhibition Strategy. *Sens. Actuators, B* **2020**, *307*, 127654.
- (82) Feifel, S. C.; Stieger, K. R.; Lokstein, H.; Lux, H.; Lisdat, F. High Photocurrent Generation by Photosystem I on Artificial Interfaces Composed of π -System-Modified Graphene. *J. Mater. Chem. A* **2015**, *3*, 12188–12196.
- (83) Luo, J.; Dong, G.; Zhu, Y.; Yang, Z.; Wang, C. Switching of Semicconducting Behavior from N-Type to p-Type Induced High Photocatalytic NO Removal Activity in g-C3N4. *Appl. Catal., B* **2017**, *214*, 46–56.
- (84) Wu, J.-B.; Lin, M.-L.; Cong, X.; Liu, H.-N.; Tan, P.-H. Raman Spectroscopy of Graphene-Based Materials and Its Applications in Related Devices. *Chem. Soc. Rev.* **2018**, *47*, 1822–1873.
- (85) Das, A.; Pisana, S.; Chakraborty, B.; Piscanec, S.; Saha, S. K.; Waghmare, U. V.; Novoselov, K. S.; Krishnamurthy, H. R.; Geim, A. K.; Ferrari, A. C.; Sood, A. K. Monitoring Dopants by Raman Scattering in an Electrochemically Top-Gated Graphene Transistor. *Nat. Nanotechnol.* **2008**, *3*, 210–215.
- (86) Shih, C.-J.; Wang, Q. H.; Jin, Z.; Paulus, G. L. C.; Blankschtein, D.; Jarillo-Herrero, P.; Strano, M. S. Disorder Imposed Limits of Mono- and Bilayer Graphene Electronic Modification Using Covalent Chemistry. *Nano Lett.* **2013**, *13*, 809–817.
- (87) Joyner, J. C.; Reichfield, J.; Cowan, J. A. Factors Influencing the DNA Nuclease Activity of Iron, Cobalt, Nickel, and Copper Chelates. *J. Am. Chem. Soc.* **2011**, *133*, 15613–15626.
- (88) Kahn, A. Fermi Level, Work Function and Vacuum Level. *Mater. Horiz.* **2016**, *3*, 7–10.
- (89) Quarti, C.; De Angelis, F.; Beljonne, D. Influence of Surface Termination on the Energy Level Alignment at the CH3NH3PbI3 Perovskite/C60 Interface. *Chem. Mater.* **2017**, *29*, 958–968.